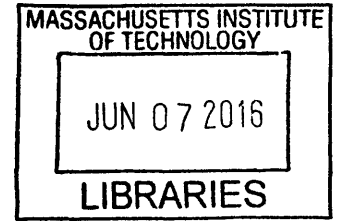# Structural Optimization of a Planar Reciprocal Frame with Triangular Topology

by

Gerry H.F. Ip

B.A.Sc., Department of Civil Engineering
University of Toronto (2015)

SUBMITTED TO THE DEPARTMENT OF CIVIL AND ENVIRONMENTAL
ENGINEERING IN PARTIAL FULFILLMENT OF THE REQUIREMENTS FOR THE
DEGREE OF

MASTER OF ENGINEERING IN CIVIL AND ENVIRONMENTAL ENGINEERING
AT THE
MASSACHUSETTS INSTITUTE OF TECHNOLOGY

JUNE 2016

© 2016 Gerry H.F. Ip. All rights reserved.

The author hereby grants to MIT permission to reproduce and to distribute publicly paper and electronic copies of this thesis document in whole or in part in any medium now known or hereafter created.

Signature of Author: _____ Signature redacted
Department of Civil and Environmental Engineering
May 10, 2016

Certified by: _____ Signature redacted
Corentin Fivet
Lecturer of Civil and Environmental Engineering
Thesis Supervisor

Certified by: _____ Signature redacted
John A. Ochsendorf
Professor of Civil and Environmental Engineering
Thesis Supervisor

Accepted by: _____ Signature redacted
Heidi Nepf
Donald and Martha Harleman Professor of Civil and Environmental Engineering
Chair, Departmental Committee for Graduate Students

Structural Optimization of a Planar Reciprocal Frame
with Triangular Topology

by

Gerry H.F. Ip

Submitted to the Department of Civil and Environmental Engineering on May 10, 2016 in Partial Fulfillment of the Requirements for the Degree of Master of Engineering in Civil and Environmental Engineering

ABSTRACT

Reciprocal frame (RF) structures consist of linear members that are mutually supporting within a closed circuit, enabling spans that are much greater than the length of an individual member. Also known in literature as 'nexorades', these geometrically complex structures offer unique architectural and structural advantages.

This thesis explores the topic of structural optimization for a planar RF floor/roof framing structure, focusing on the triangular RF topology. The relative structural performance of the grids is computed and plotted against the geometric parameters for various load cases. The two key parameters studied are the rotation angle of the members which defines the geometry, and the total number of members in the grid which defines the grid density. The load cases modelled include both symmetric and asymmetric loading scenarios on a hypothetical surface supported by the grid, and therefore the loads are distributed to the members based on tributary areas. The goal of this thesis is to determine whether certain geometries will be more favorable across multiple load cases, or whether the optimal geometry would vary greatly. The structural performance is defined by the total strain energy in the grid.

Results show that smaller rotation angles at the unit RF level produce more structurally efficient RF grids. Depending on the grid density and load case, the optimal angle lies between 4 and 8.2 degrees. It is found that the optimal angle remains relatively unchanged for a given grid density between the symmetric and asymmetric load cases.

Thesis Supervisor: Corentin Fivet
Title: Lecturer, Civil and Environmental Engineering

Thesis Supervisor: John A. Ochsendorf
Title: Professor, Civil and Environmental Engineering and Architecture

Acknowledgements

I would like to thank Dr. Corentin Fivet for taking the time to understand my research interests and introducing me to the intriguing subject of reciprocal frame structures. Dr. Fivet has been of immense support throughout my year at MIT, both as my thesis advisor and as my go-to advisor for any structural engineering inquiries I have from other coursework. I am grateful for his generosity in always being available for us.

I would also like to thank Professor John Ochsendorf for providing constructive feedback on this thesis, and for his patience and kindness throughout the year. Professor Ochsendorf has always been on the lookout to bring the next leading structural engineer to MIT for our class to learn from, and the experience has been rewarding.

Thank you to my great classmates: I couldn't have asked for a better group of friends to spend the days and nights with in the MEng room.

Finally, thank you to my family for their love and support throughout my academic endeavors, and to my friends in Canada for their continued moral support.

Table of Contents

List of Figures

List of Tables

1. Introduction

Reciprocal frame (RF) structures consist of linear members that support one another within a closed circuit, hence the origin of the term "reciprocal". This mutually supporting nature of the structure enables spans that are much greater than the length of an individual member. RF structures have also been referred to in literature as 'nexorades', where each member is termed a 'nexor', meaning 'link' in Latin (Baverel 2004).

1.1. Background

As Larsen (2008) suggests in her work "Reciprocal Frame Architecture", it is difficult to pinpoint exactly when the first RF structure was built. Evidence of historic structures that bear similarity to RF principles can be found in both Japanese and Western architecture, dating as early as the 12th century. For example, 13th century medieval architect Villard de Honnecourt created sketches of a planar floor beam grillage that closely resembles a planar rectangular RF grid (see Figure 1-1). Honnecourt's sketches reflect a solution to resolving the problem of spanning a space with members shorter than the required span, as buildings became increasingly larger.
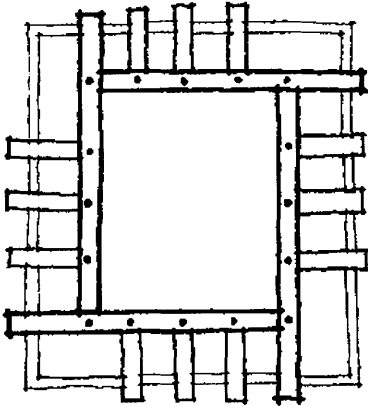
Figure 1-1 - Honnecourt's planar grillage assembly (sketched by A.E. Plroozfar) (Larsen 2008)..

An RF structure can often be decomposed into a basic repeating unit, which will be referred to in this thesis as the "unit RF". A unit RF is comprised of at least three members arranged in a radial manner such that they circumscribe a polygon, hence forming the closed "circuit". Depending on the arrangement of the members, this polygon may be regular or irregular, as seen

in Figure 1-2. Therefore, it is possible to have RF structures with varying geometries, and with varying complexity depending on the regularity of the polygon and tessellation (see Figure 1-2). A further level of complexity can be created in "complex RFs", where smaller unit RFs are embedded within larger units. The connection between members in a simple reciprocal frame is facilitated by pressure and friction, but in practical applications the members are often tied or notched (Larsen 2008).
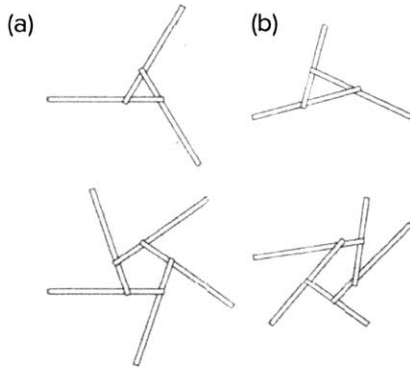
Figure 1-2 – Regular unit RFs (a); Irregular unit RFs (b) (Kohlhammer and Kotnik 2011).
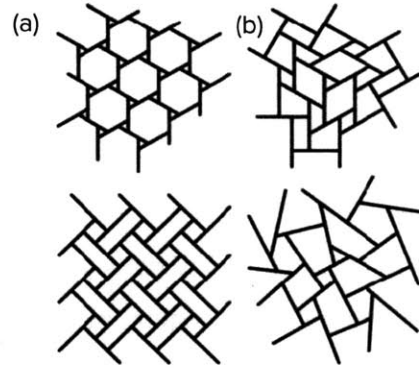
Figure 1-3 - Regular RF grids (a); Irregular RF grids (b) (Kohlhammer and Kotnik 2011).
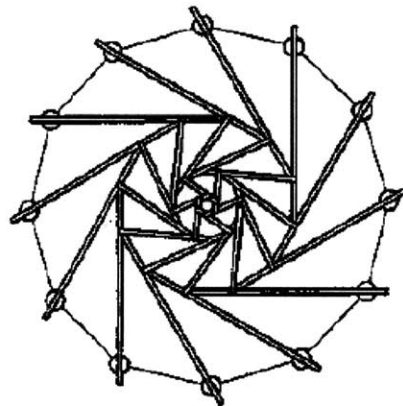
Figure 1-4 - Example of a complex RF (Larsen 2008).

Reciprocal frames are often sloped by its reciprocal nature, as the stacking of members on top of each other naturally creates a gradient. The offset distance between the centerline of two connected members is also known as the "eccentricity". The sloped nature of RF structures makes them particularly suitable in roof applications, though flat RF structures are also possible through notching. In the flat configuration, the members primarily transfer loads in bending, while in an

14

eccentric configuration, loads are transferred through both axial and bending. Built examples of RF structures commonly employ timber, as it is an inexpensive material that is easy to work with during construction due to its smaller size, is easily notched, and has generally good behavior in bending (Larsen 2014).

The Seiwa exhibition hall in Japan is an excellent built example of both sloped and flat RF structures, utilizing timber as the structural material (see Figure 1-5 and Figure 1-6). Upon entering the exhibition hall, one would find themselves underneath multiple RF structures: first, there are the 12 spiraling roof beams, which are in turn supported by another two sets of flat RF beams that spiral in opposite direction (Larsen 2008).

Figure 1-5 - Interior of the Seiwa exhibition hall (Larsen 2008).
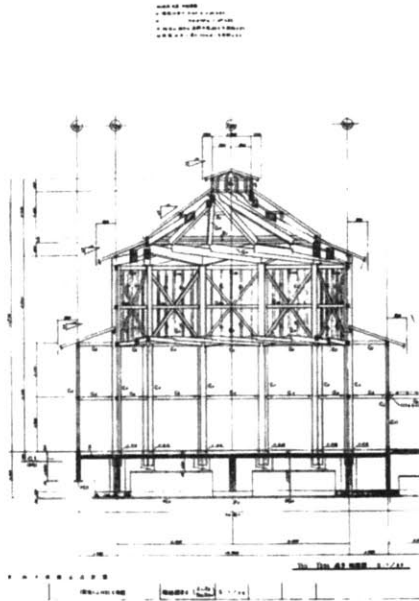
Figure 1-6 - Section drawing of the Seiwa exhibition hall (drawn by Tadashi Hamauzu) (Larsen 2008).

In addition to having obvious architectural benefits, reciprocal frame structures also offer advantages structurally. The polygonal and circular nature of RF structures produces plan forms that depart from traditional rectangles, and curved forms can be generated with straight members. The latter is particularly advantageous, given that curved timber members are often difficult to manufacture. Connections in an RF structure are relatively low-tech and highly repetitive in symmetrical grids, thus simplifying construction. The repetition of short members of equal length are also advantageous from both a cost and constructability perspective. Finally, studies have

15

shown that complex RF structures have a high degree of redundancy, as load tests to failure demonstrated their ability to find alternative load paths (Larsen 2014).

The unique characteristics of RF structures have made them of interest in applications beyond conventional structures, such as in the design of recreational pavilions and emergency deployable structures. The Kreod Pavilion constructed for the London 2012 Olympic Games is an example of how a timber RF structure is a great fit for structures that need to be easily constructed and disassembled (see Figure 1-7). With the connections inspired by those from furniture, assembling and disassembling the joints was greatly simplified, while simultaneously achieving an aesthetically pleasing and curvaceous geometry (Larsen 2014).

Recognizing the compatibility of timber as an inexpensive structural material for RF structures, and the ability of RF structures to be quickly constructed from identical members of equal length, Larsen (2013) explored the possible use of RF structures as emergency structures. Her research proposed three possible typologies of emergency RF structures: a deployable "arch" type system; a "planar" frame system, and a "hanging" type system. In the "arch" type system, a series of arches would be individually assembled and then connected to each other by cables and fabric. Upon tensioning the cables, the structure would unfold and create an enclosed space (see Figure 1-8). In the "planar" frame system, a rectangular shelter would be created with walls, floors, and ceilings constructed from a planar RF grid (see Figure 1-9). Finally, the "hanging" type system consists of hanging an RF grid from a series of supports to create an overhead shelter (see Figure 1-10). All of these systems benefit from the simplicity of connections, use of low-tech equipment, and repetition of member sizes and lengths.
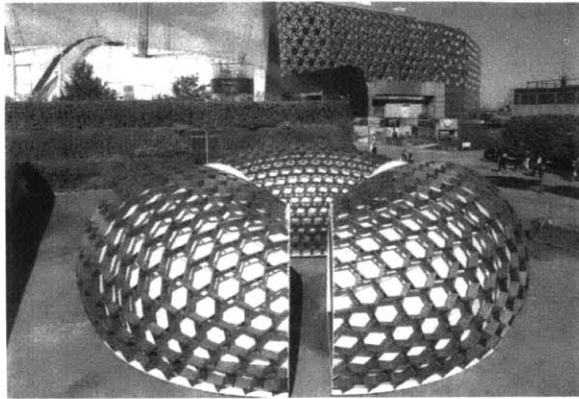
Figure 1-7 - Kreod Pavilion (Kingsford).
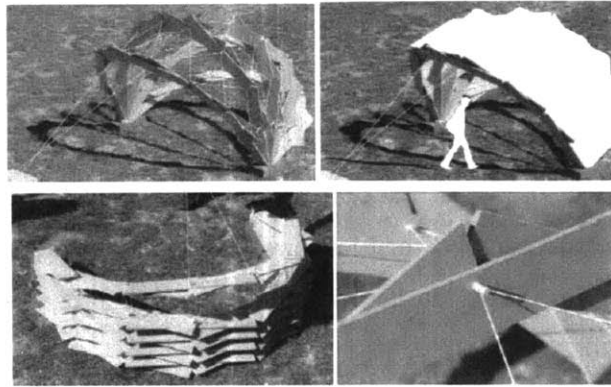
Figure 1-8 - An "arch" type deployable emergency RF structure (Larsen and Lee 2013).
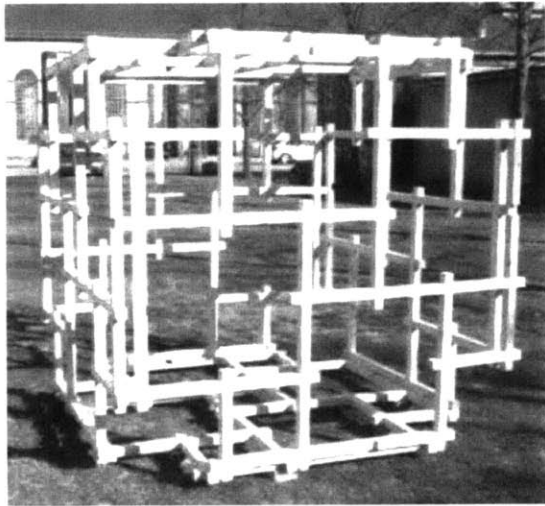
Figure 1-9 - A "planar" type emergency RF structure (Larsen and Lee 2013).
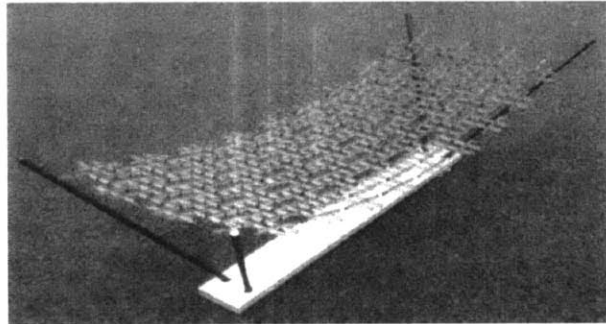
Figure 1-10 - A "hanging" type emergency RF structure (Larsen and Lee 2013).

1.2. Problem Statement

The topic of structural optimization has garnered interest in recent years, which can be attributed to the increased awareness of environmental sustainability in structural design, and how efficient structures can reduce the carbon footprint through minimizing material quantities. The latter is particularly powerful when faced with the statistic that more than 50% of a structure's total carbon footprint during its lifetime can be the embodied carbon of its structure (Kaethner and Burridge 2012).

Given that RF structures can come in a wide variety of topologies, geometries, and forms, what constitutes as an "optimal" RF structure is not well understood yet. The motivation behind this topic is to benefit the practical application of RF grids as a floor or roof framing structure, with the aim of generating results that will serve as useful rules of thumb for designers who are contemplating the use of a planar RF grid in their structure. Therefore, the question is whether there is a particular RF grid geometry for the triangular topology that is optimal across both symmetric and asymmetric load cases.

This thesis continues research on how geometry impacts the structural efficiency of an RF structure. The thesis focusses on a planar RF grid with a triangular topology, which consists of 3 members at the unit RF level. The goal is to determine what the optimal geometry is for various load cases, and whether this optimal would vary greatly across the different load cases. The geometry of an RF grid is defined by two variables; the rotation angle of the members, which dictates the size of the engagement window (see Figure 1-11), and the density of the grid, which dictates the number of members comprising the grid. The three smallest possible grid densities are explored: the first with 12 members in total, or 6 unit RFs; the second with 42 members (24 unit RFs), and the third with 156 members (96 unit RFs). In this thesis, the grid densities are referred to by the number of unit RFs they consist of (i.e. N = 6, N = 24, N = 96).

The load cases considered have been chosen based on possible real-world loading scenarios, on the assumption that the RF structure will be supporting a flat roof or floor surface. Both symmetric and asymmetric load cases are analyzed, which are summarized in Table 1-1 and represented in Figure 1-12. All load cases include the self-weight of the members. The area loads are applied on the members as discretized point loads and distributed by tributary area, and the self-weight is applied as a uniform line load on the members. The joints between members are

18

assumed to be notched connections and therefore are pin connections. The boundary support conditions are rollers, except for one pin for lateral resistance. Lateral loads and torsion are not considered in this thesis, and only linear elastic behavior is assumed in the analysis. Since the grid is planar, the primary structural action is in bending.
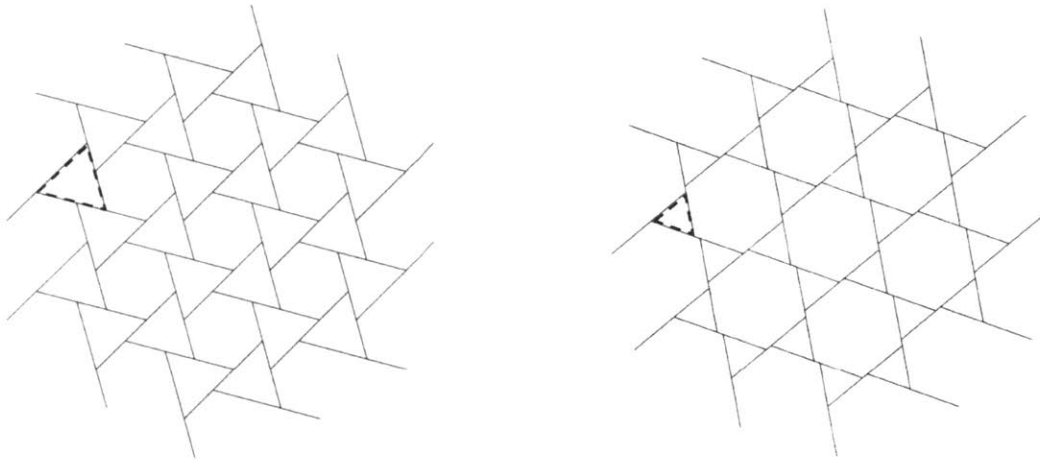
Figure 1-11 - N = 24 grids with varying rotation angles.
The engagement window is highlighted with a dotted triangle.

Symmetric Load Cases	LC 1. Uniform area load + self-weight
	LC 2. Uniform area load with concentrated load at center + self-weight
Asymmetric Load Cases	LC 3. Uniform area load with concentrated load at midpoint between center and support + self-weight
	LC 4. Uniform area load on half of grid + self-weight

Table 1-1 - Summary of load cases.
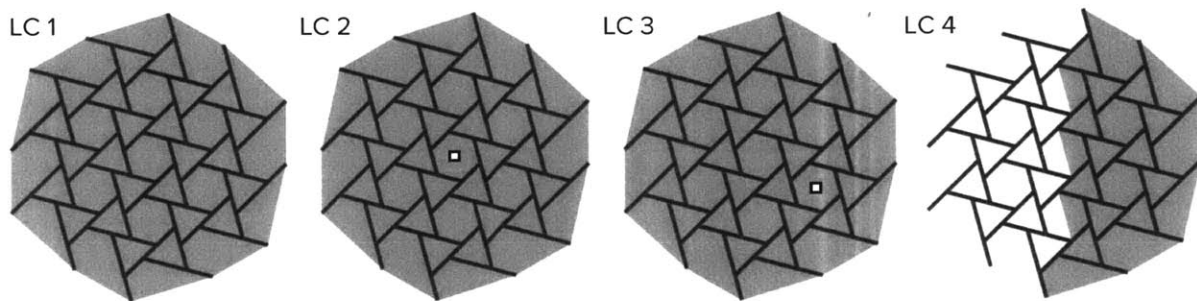
Figure 1-12 - Schematic of applied loads, as shown on the N = 24 Grid.
Shaded area indicates extent of area load; point indicates location of concentrated load.

2. Literature Review

Despite being a structural system that has been around for centuries, reciprocal frame structures have not been commonly adopted in practice. Researchers suggest that it is likely because their structural behavior was never well understood. Structural systems are often selected for a given design problem on the basis of appropriateness given the loading conditions, span requirements, and architectural goals. As Parigi & Kirkegaard (2013a) note, it is unclear under what circumstances would a reciprocal frame be a good fit as a structural system. Therefore, several studies in recent decades have sought to better understand the structural behavior of RF structures.

Gelez, Aubry & Vaudeville (2011) studied planar RF grids with the rectangular topology, with the aim of better understanding their structural behavior in order to facilitate their design. In their study, they proposed two mathematical formulas pertaining to the structural analysis of a given RF grid: one that provides the value of maximum bending moment, and another that provides the value of bending moment and deflection at any location. The loads applied were vertical point loads (see Figure 2-1). They also compared the structural behavior of the RF grid to an equivalent flat grid, and found that the RF grid was not competitive with respect to bending moments and deflections. However, the distribution of bending moments was more even in the RF grid, and when subjected to an irregular perimeter geometry, the RF grid performed better in terms of distributing the support reactions (see Figure 2-2). Therefore, they concluded that despite the disadvantages of the rectangular RF grid in terms of required stiffness and strength, there are benefits to their application in certain situations that require irregular perimeters, and low sensitivity to settlements, local thermal loads, or global thermal loads.

Figure 2-1 - Example of an RF grid with rectangular topology studied by Gelez et al (2011).
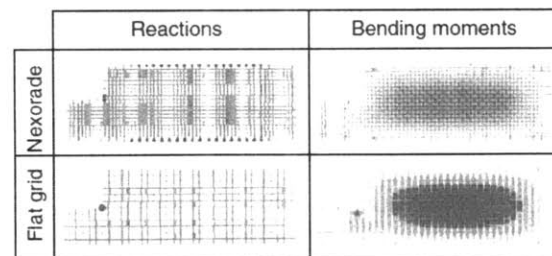
Figure 2-2 - Comparison between an RF grid and a regular grid for an irregular perimeter (Gelez, Aubry, and Vaudeville 2011).

Parigi & Kirkegaard (2013a) studied the structural efficiency of various 2D and 3D RF configurations with the triangular topology. Their research is the most relevant to this thesis, as they were also interested in exploring the effect of geometric parameters on structural performance. Parigi & Kirkegaard studied 8 different RF geometries, both in 2D as flat grids and also in 3D by varying the eccentricities of the members (see Figure 2-3). The structural efficiency of each was taken as the value of maximum stress and displacement, and the two load cases consisted of a uniform line load on each member (symmetric), or a uniform line load on half of each member (asymmetric).
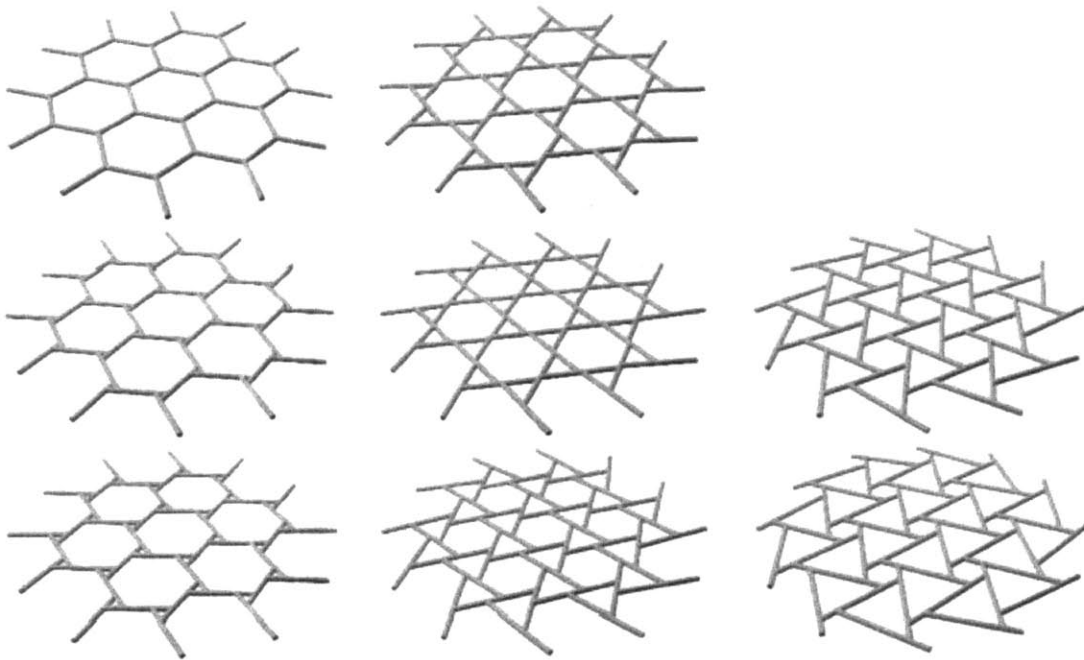
Figure 2-3 - Planar RF grid configurations studied by Parigi and Kirkegaard (2013a).

Although this thesis is similar in principle to the research performed by Parigi & Kirkegaard (2013a), it addresses some of the points for future work that was suggested in their research, and therefore differs by a few key aspects. The first is the use of global values such as total strain energy in assessing the structural performance, as opposed to the local values of maximum stress and displacement. Using global values would better capture the efficiency of the structure as a whole, because it would account for the contributions each member has in the performance of the grid. A downside to considering simply the value of maximum stress in the grid is that it only reflects what is happening at a single member level, and does not reflect the stress distribution among other members. Therefore, the evaluation of structural efficiency

utilizing the total strain energy is expected to produce more representative results on the performance of the entire structure.

The second suggested point for future work that is addressed in this thesis is the consideration for pin connections between elements. In their research, Parigi & Kirkegaard (2013a) only modelled the joints between members as fixed, which would unlikely be the case in reality as there would be some rotational freedom between the members.

A final difference in the methodology is the modelling of the loads. In this thesis, load cases that represent possible loading scenarios in reality are considered, as the structure is considered to be a hypothetical structural floor framing system. The loads are therefore distributed onto the members by tributary area, which contrasts with previous work as the members would receive non-uniform linear loads.

Kirkegaard and Parigi (2013b) also explored the topic of robustness for reciprocal frame structures. They hypothesized that RF structures would be prone to progressive collapse due to the mutually supporting nature of the members; however, the results from their research proved otherwise. They found that RF structures are capable of redistributing the loads when subject to a loss of a member or a support, but that the sensitivity of a structure to a failure depends on where the failed member occurs. With the requirement of robustness being specified in most building codes across the globe, the application of an RF as a structural system could therefore constitute as a method of addressing this requirement, since it involves "selecting a structural form that can survive the accidental removal of an individual member or limited part of the structure" – one of the robust design principles outlined in the Eurocode.

3. Methodology

This section outlines the methodology used to generate the parameterized structural analysis models of the reciprocal frame structures. Although the geometry of RF grid structures may appear complex, parameterizing the structural analysis model of a regular RF grid is a relatively straightforward task, and is summarized with a flow chart in Figure 3-1. Grasshopper, a graphical algorithm editor for Rhino, a 3-D modelling software, is the primary software utilized in this thesis (Robert McNeel & Associates 2016). Custom components created through the GhPython plugin for Grasshopper are also used extensively, and are comprised of custom scripts written in the Python programming language (Robert McNeel & Associates 2014). Structural analysis is performed using the Karamba plugin for Grasshopper (Preisinger 2016). A hand calculation procedure used to verify the Karamba analysis outputs is also described in this section. The hand calculation is done to ensure the credibility of the computer analysis outputs.
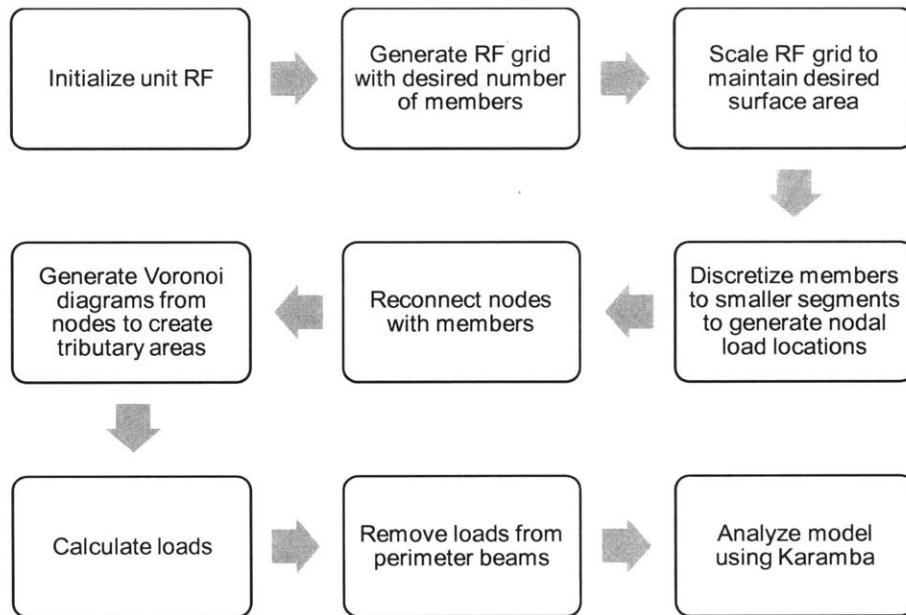
Figure 3-1 - Sequence of methodology used to generate parameterized model.

3.1. Generating Typology

The first step is to generate the unit RF, which is initialized as an equilateral triangle. Each side of the triangle represents a member, and each vertex is considered to be the starting point of one member. To generate the reciprocity, the members are rotated clockwise by an equal angle about its starting point (see Figure 3-2). This reduces the size of the "triangle" within the unit RF, known as the engagement window as mentioned in Section 1.2. The side length of this triangle is defined as the engagement length. By increasing the rotation angle, the engagement length decreases. This rotation angle will serve as the key variable in the optimization process; the resulting geometries will be defined by this rotation angle. The rotation angles considered are 0 to 30 degrees in 0.1 degree increments. In addition, the engagement length for each rotation angle will normalized in this thesis and presented as an "engagement ratio", since the engagement length would scale according to the size of the initial unit RF; we are only interested in the ratio of this length to the overall member length.
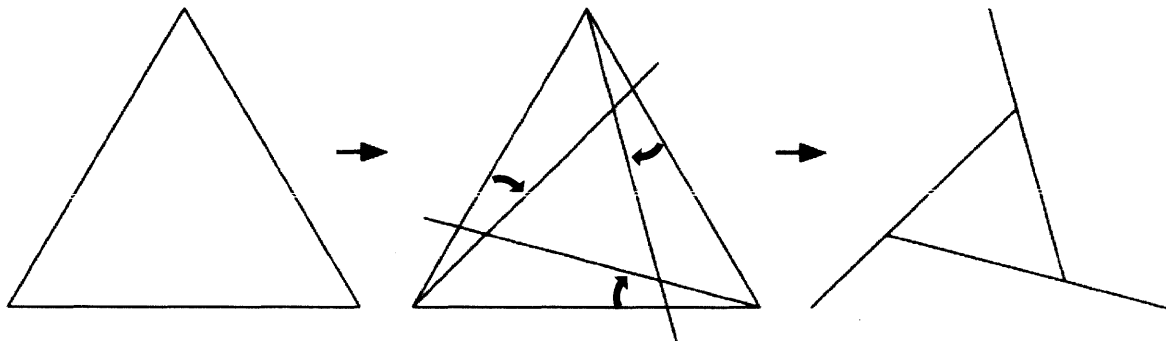
Figure 3-2 - Generating the unit RF.
A rotation angle of 15° is pictured. The overhanging portions are trimmed after rotating the members.

Once the unit RF is generated, the RF grid typology with the minimum number of members can be created using a polar array. As depicted in Figure 3-3, the length of a member that is outside of the engagement window is named the "outer length". Rotating this outer length 60 degrees counter-clockwise about the vertex of the engagement window would pinpoint the center of the array. Once the center is found, the unit RF is then arrayed 60 degrees apart until a full circle is achieved – which means that the smallest RF grid is comprised of 6 unit RFs. This is due to the nature of RF grids needing to form closed circuits. Larger grids can then be created using the same procedure of polar arraying successively larger grids, as demonstrated in Figure 3-4. Three separate models are created to explore the three different grid densities (Figure 3-16).
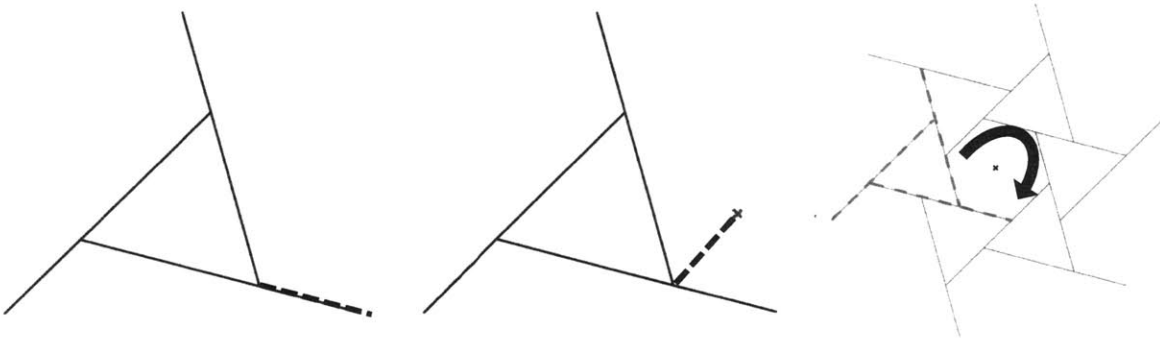
Figure 3-3 - Diagrammatic procedure of generating the N = 6 Grid.
A unit RF with the "outer length" highlighted (left); Outer length rotated by 60 degrees to get center of array
(center); Grid generation following polar array (right).
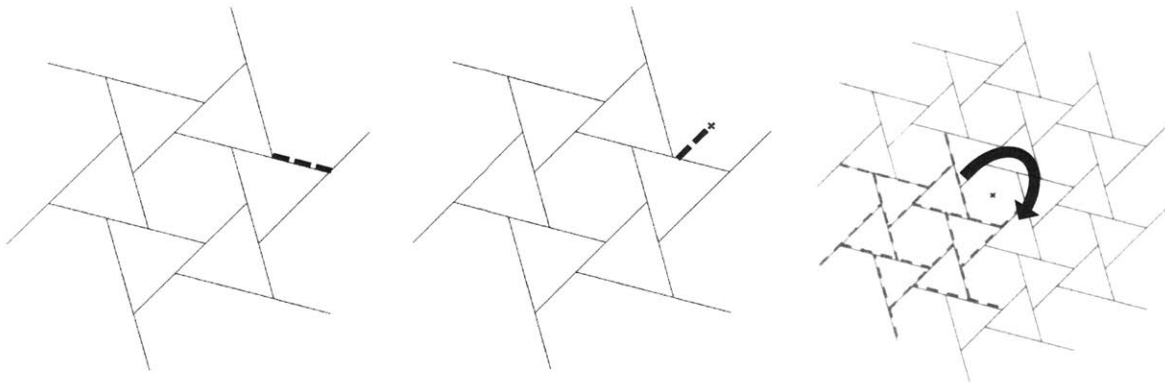
Figure 3-4 - Diagrammatic procedure of generating the N = 24 Grid.

The total number of RF units (N) in a grid can be calculated from Equation 1, based on the number of rotational arrays (n) needed to attain the grid. For example, the next grid size up from the base N = 6 grid would be N = 24, since two arrays are needed (first to generate the N = 6 grid, and second to generate the N = 24). The N = 96 grid is therefore generated from three arrays.

$$N = 6 * 4^{n-1} \tag{1}$$

Due to the self-supporting nature of a reciprocal frame, a connection point between two members result in one of the members being supported or supporting the other. In an RF grid with triangular topology, the supported vs. supporting conditions for each connection point in a given member is straightforward, as there are only two types of members. An interior member is always supported on its ends and supporting two along its span, and the exterior members connecting to the supports are always supported on both ends and supporting one member along its span (see Figure 3-5). A plan view schematic of the supported vs. supporting conditions at each joint is shown in Figure 3-6. For any given vertical load on a member, the load will be resisted in bending

27

and travel to the nearest supporting member, continuing this process until it reaches a boundary support at the outermost members.

Exterior Member

Interior Member
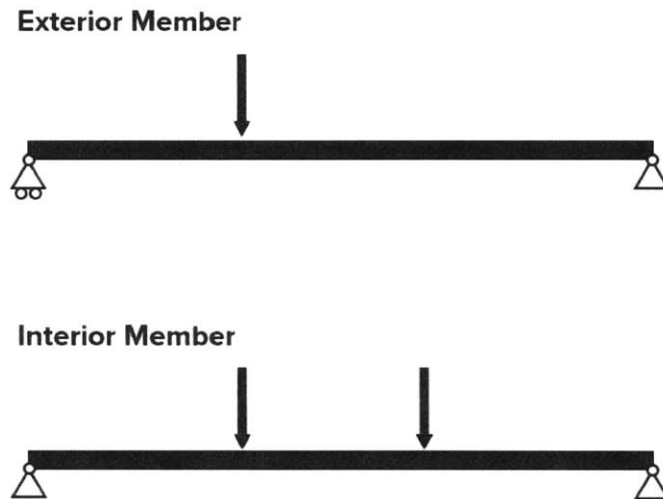
Figure 3-5 - Support conditions of members in an RF grid.
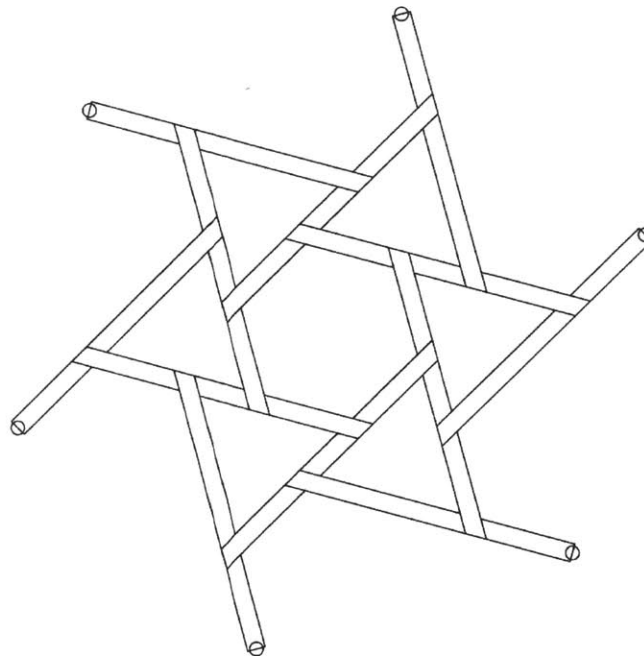
Figure 3-6 - Plan view of N = 6 grid showing the support conditions for each member.
Note which members are on top at each connection point. Circles indicate boundary supports.

Examples of the N = 24 grid at various rotation angles are shown in Figure 3-7. Note the decrease in the size of the engagement window (decrease in engagement ratio) as the rotation angle

increases; this relationship between rotation angle and engagement ratio remains for all grid densities.

Angle: 0°
Engagement Ratio: 1.00

Angle: 5°
Engagement Ratio: 0.91

Angle: 10°
Engagement Ratio: 0.79

Angle: 15°
Engagement Ratio: 0.67

Angle: 19.1°
Engagement Ratio: 0.56

Angle: 20°
Engagement Ratio: 0.54

Angle: 25°
Engagement Ratio: 0.42

Angle: 30°
Engagement Ratio: 0.00
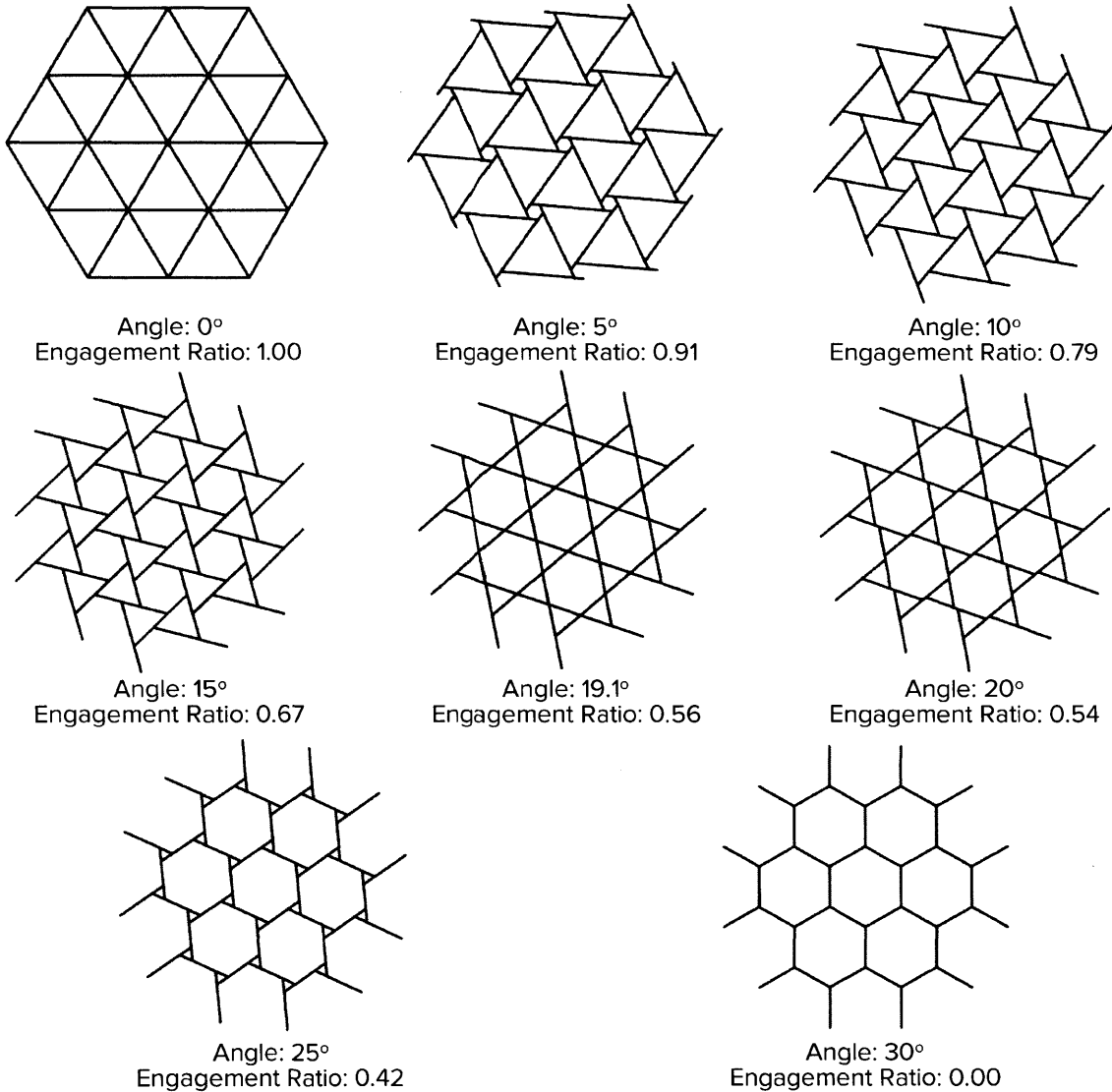
Figure 3-7 - Examples of the N = 24 grid at various rotation angles.

It can be observed that a rotation angle of 0, 19.1, or 30 produces a structure that does not behave in a reciprocal manner, since the members would either align with one another and therefore not support each other in a complex manner (at 0 and 19.1 degrees), or multiple members would converge at a single node (at 30 degrees) which also would not permit reciprocal behavior. These results are referred to as non-reciprocal grids and are omitted from the possible range of rotation angles.

29

3.2. Maintaining Desired Surface Area

The third step is to scale the RF grid to obtain the desired surface area of the floor or roof framing structure. This is because for a given initial length of members at the unit RF level, the surface area of the RF grid changes as the rotation angle changes. Therefore in order to maintain a constant coverage area, the parameterized model needs to be scaled to the correct size for each rotation angle, after the polar arraying process.

In this thesis, the surface area is the area bounded by the perimeter beams (see Figure 3-8). The area is taken to be the equivalent of a circular space with a radius of 5 m, which leads to an area of 78.54 m^2. The resulting span is approximately 10 m. The surface area is maintained across all grid densities in order to compare the effect of grid density for a fixed floor or roof area.
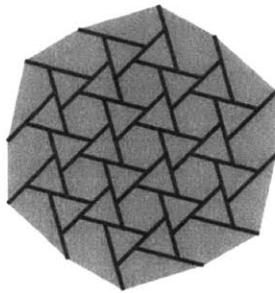
Figure 3-8 - Diagram indicating the surface area of a grid (shaded).

3.3. Discretization of Members for Loading

The fourth step is the discretization of members to smaller segments. This step is needed due to complications in utilizing the Mesh Load component in Karamba to translate area loads into distributed line loads on members (Preisinger 2016). As a result, distributed loads are discretized as closely spaced point loads. In order to apply point loads along the length of a member in Karamba, a physical node must exist at the point load location. Hence, the members are divided into segments of equal length to generate the nodes, and a custom component is coded to re-draw the members between the nodes. The node spacing is set to 0.1 m, as it was found that nodes too close together could lead to bugs when generating Voronoi diagrams, which are needed for proper calculation of the tributary areas. The bug causes the tributary areas to overlap, which leads to an improper calculation of the tributary areas (see Figure 3-9).
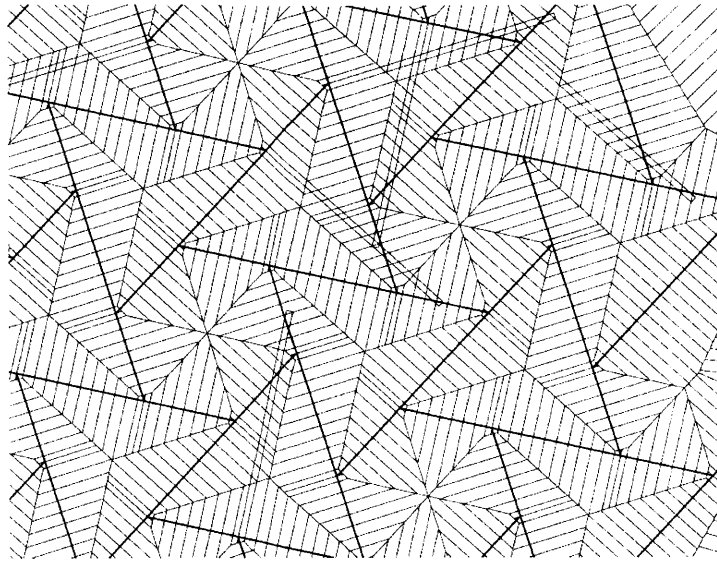
Figure 3-9 - Example of the Voronoi bug.
Note the overlapping of tributary areas at certain locations.

The custom component of re-drawing the members is a key part of the parameterized model, as it requires properly indexing which members one connects to, and the locations at which the connection happens. The re-drawing is also necessary as it ensures that the connection between two members is appropriately modelled with a node that is shared between the two – otherwise the Karamba analysis would not work.

Depending on the rotation angle, the node which connects a member with another may lie very close to one of the discretized nodes on the supporting member (see Figure 3-10). This may once again lead to glitches in generating the Voronoi diagrams as mentioned previously. Therefore, a custom component was written such that one of the nodes among the two within close proximity would be removed.
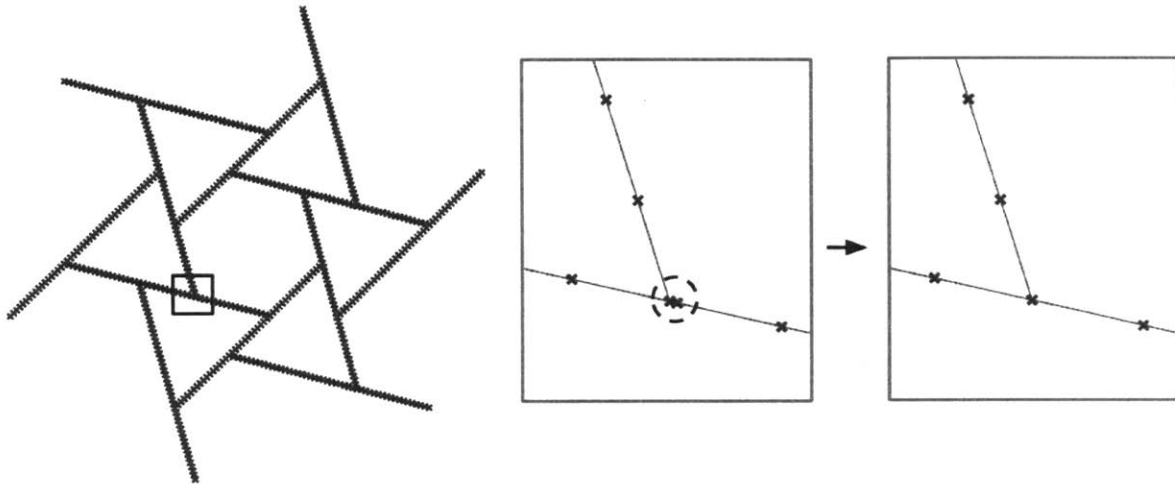
Figure 3-10 - Example showing the removal of nodes in certain cases.

Once the points in the model are generated, they are input into the Voronoi component in Grasshopper to generate Voronoi diagrams, which delineate the tributary areas of each respective point (see Figure 3-11) (Robert McNeel & Associates 2016). For the case of area loads, the magnitudes of the loads to be applied is determined by multiplying each tributary area by the load per unit area. The result is an approximated distributed load on the members that has been discretized as point loads and is non-uniform (see Figure 3-12). Nodes from perimeter beams that span between support points are also included in the Voronoi component in order to properly determine the tributary area of the members, but the structural analysis of the beams are omitted in the results. This is because we are only interested in the performance of the grid itself.
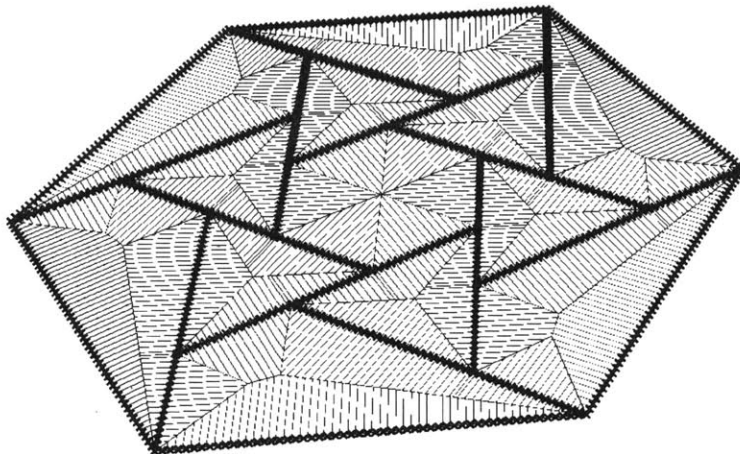
Figure 3-11 - Tributary areas.
The hexagonal perimeter nodes are only used to generate the tributary areas and have no applied loads.
The analyses of the perimeter beams are neglected.

32
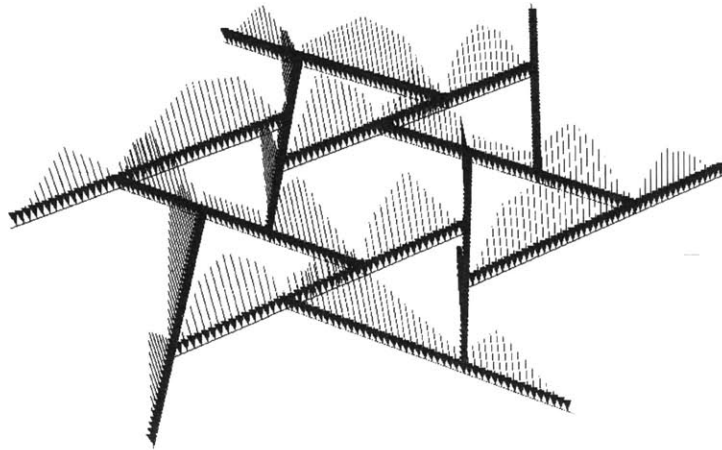
Figure 3-12 - Discretized distributed loads.

3.4.   Generating Different Load Cases

For the different load cases, the procedure for applying the loads remains similar. In the case of applying a concentrated load, the relevant tributary areas are trimmed from the entire Voronoi diagram (see Figure 3-13), and the magnitude of point load to be applied on each node is calculated based on the proportion of its tributary area to the total trimmed area. The calculated loads are then added to the load of the relevant node in the base Voronoi diagram.

In the case of a partial area load, a similar process of trimming the entire Voronoi diagram is used. For load case 4 where only half of the gird surface is loaded, a kinked dividing line following the member paths is utilized instead of dividing the grid in half with a straight line (see Figure 3-14). This is due to the nature of the applied loads being indexed to the discretized nodes along the members; following the members would allow the nodes with removed or reduced loads to be easily indexed. The resulting sum of the forces applied on the trimmed half segment remains very close to 50% of the sum in the entire area case, with only a maximum difference of approximately -0.11% depending on the rotation angle.
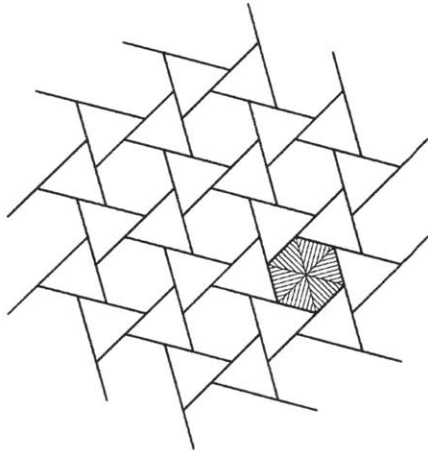
Figure 3-13 - Trimmed Voronoi diagram for distributing the concentrated load in Load Case 3.
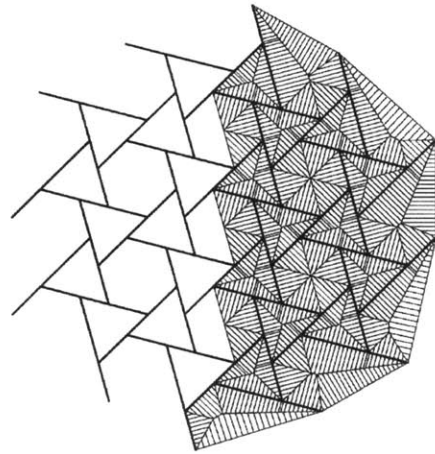
Figure 3-14 - Trimmed Voronoi diagram for Load Case 4.

3.5. Dimensioning and Self-Weight of Members

The self-weight of the members is applied as a uniform line load on the members (see Figure 3-15), which is calculated based on the cross-sectional area multiplied by the material density. The material density is 6.0 kN/m^3, based on the default value for wood in Karamba (Preisinger 2016). The members are assumed to be solid wood members with a constant cross-section across its length.
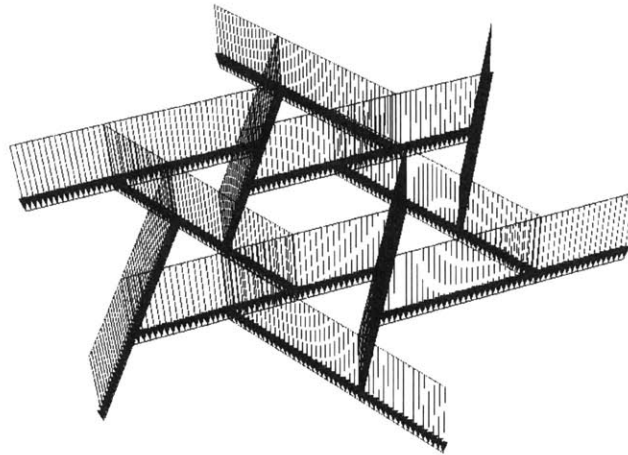
Figure 3-15 - Uniform line loads for self-weight.

The cross-section dimensions for each grid density vary because the members have been sized according to the maximum moment of all load cases at any rotation angle (i.e. for each grid density they are sized for the least-optimal rotation angle of the highest load case). This is done to

34

avoid errors in the computer analysis, as the results could be erroneous if the utilization of a member (which is primarily due to bending) greatly exceeds 1.0. Another benefit to maintaining a constant cross-section across all rotation angles is that the optimization process can be linearized, as the "optimal" would only be defined by geometry and not also the self-weight.

The member sizes for each grid density are shown in Table 3-1. The width has been held constant, while the depth changes according to the maximum moment for any rotation angle in load case 2 (the highest loading demand). Therefore, the members have been sized according to strength requirements. The required width is calculated from Equation 2, where M_r is the required moment resistance, F_y is the tensile yield stress of the material, and b is the member width. The tensile yield stress is 13 MPa, based on the default value for wood in Karamba (Preisinger 2016). This value corresponds roughly to the tensile strength parallel to the grain of a type C22 softwood species in EN 338-2003, which contains the strength properties of structural timber (European Committee for Standardization 2003). The cross-section size is the same across the entire length of the members.

$$h = \sqrt{\frac{6 * M_r}{F_y * b}} \tag{2}$$

	N = 6 Grid	N = 24 Grid	N = 96 Grid
Member Width [in]	6	6	6
Member Height [in]	28	30	17

Table 3-1 - Member dimensions for each grid density.

As it is found that the bending moment tends to increase greatly towards higher rotation angles for the two denser grids, the maximum moment used for sizing is capped off at around 27 degrees, beyond which it increases much greater than the typical increment.

Since the chosen dimensions have an impact on the self-weight of the members, which in turn impacts the magnitude of the bending moments in the members, the results could be affected as the sizing for each rotation angle is not optimized for its own bending demand (i.e. an unnecessarily high self-weight moment could skew the efficiency of a geometric configuration). To ensure this is not the case, the member depth for the rotation angle with the lowest maximum bending moment in load case 2 (4.7 degrees) was optimized for its own maximum moment, and

this value was compared with its maximum moment under the non-optimized dimension. Load case 2 is utilized because it is the expected worst-case. It would not be rational to optimize a member under load case 4 since it would have lower moments.

The result in Table 3-2 shows that the self-weight has minimal effect on the maximum moment for a given rotation angle, as the difference in moments between the optimized and non-optimized dimensions is less than 10%. This means that the size of the members has a small impact on the optimum angle. Although the member depths appear large, they are somewhat arbitrary as they are affected by the defined span and the material properties. Similar results would be obtained with smaller sections if the span was reduced or if a different species of timber was used.

	Non-Optimally Sized	Optimally Sized	Difference
Member Depth [in]	30	17	-
Max. Moment (without self-weight) [kNm]	51.3	51.3	-
Max. Moment (incl. self-weight) [kNm]	61.1	56.9	-7.47%

Table 3-2 - Effect of self-weight on the max. bending moment at 4.7 degrees (N = 24 grid).

Finally, although the parameterized structural model is a stick model where the members have been idealized as lines without thickness, it is important to note the implications of member width on possible geometries. For certain rotation angles where the connection points are in close proximity, the member width must be taken into account in reality as the members cannot overlap. However, since the actual member widths have been arbitrarily chosen in this thesis and could vary in reality, the rotation angles leading to an overlapping of members are still included in the results. Overlapping does not negatively affect the analysis results since the analysis model is a stick model – the cross-sections are only used to compute strength, deflections, and weight.

3.6. Summary of Loads

The magnitudes of the applied loads for all load cases are tabulated in Table 3-3 and Table 3-4. The live loads are based on un-factored load values for the critical expected occupancy, which is assumed to be a floor framing structure supporting an assembly area. The values are referenced from the Minimum Design Loads for Buildings and Other Structures, ASCE 7-10 (American Society of Civil Engineers 2013).

LC 1 – Uniform Load	4.8 kPa (100 psf)
LC 2 – Uniform Load + Concentrated Load	4.8 kPa (100 psf) + 8.9 kN (300 lbs)
LC 3 – Uniform Load + Concentrated Load	4.8 kPa (100 psf) + 8.9 kN (300 lbs)
LC 4 – Uniform Load on Half	4.8 kPa (100 psf)

Table 3-3 - Magnitude of live loads for all grid densities.

	N = 6 Grid	N = 24 Grid	N = 96 Grid
Self-Weight [kN/m]	0.650	0.697	0.395

Table 3-4 - Magnitude of dead loads for each grid density.

3.7. Structural Analysis

The final step is to analyze the parameterized structural model, utilizing finite element analysis implemented via the Karamba plugin for Grasshopper (Preisinger 2016). Inputs that are needed to assemble the structural model include the geometry, boundary support conditions, joint conditions, loads, member cross-section, and material properties. The joints at the member connections are modelled as pins, as it would be difficult to achieve full fixity of the connection in reality. The boundary support conditions are also pins.

The total strain energy of the model is then calculated using Equation 3, where E is the modulus of elasticity, and I is the moment of inertia for the strong axis. E is taken as 10,500 MPa, based on the default value for wood in Karamba (Preisinger 2016). Since the cross-section size is held constant across the entire member length at every rotation angle for a given grid density, EI would be constant, and consequently the strain energy is only proportional to the sum of the maximum moments squared in each member (Equation 4). The sum of the maximum moments squared is therefore the metric for structural performance, and is referred to as the Strain Energy

Factor. It is independent of the material cross-section, and is solely dependent on geometry. Note that a lower value for the Strain Energy Factor corresponds to a more efficient geometry.

$$\text{Strain Energy} = \sum \frac{Mmax_i^2}{2EI} \tag{3}$$

$$\text{Strain Energy Factor} = \sum Mmax_i^2 \tag{4}$$
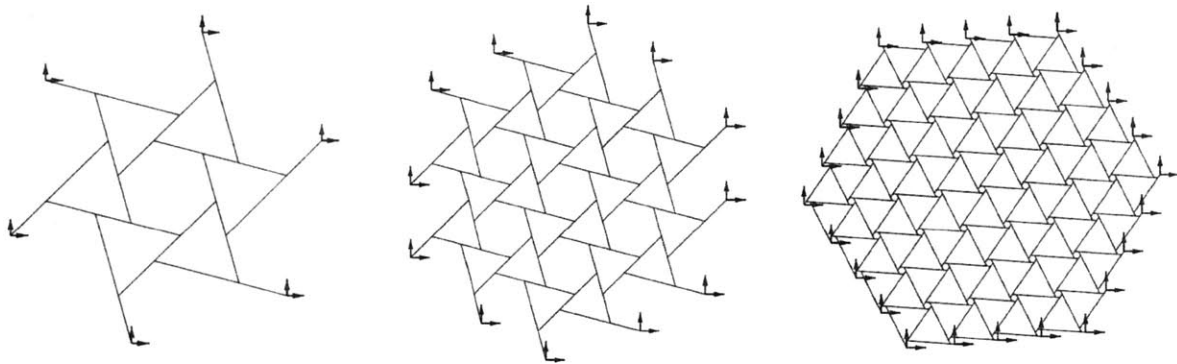
Figure 3-16 - Structural model of the 3 different grid densities.
The arrows at the on the members indicate the support locations.

3.8. Categorization of Member Types

Due to the symmetry of the RF grid, certain members have an identical load distribution when the structure is loaded symmetrically. For example, the N = 6 grid has two types of members, where the members of each type receive identical loading (see Figure 3-17). Therefore, it is possible to categorize members in an RF grid based on their load distribution, which corresponds to their relative location and topology. As grids become progressively denser, the number of different member types would increase: for the N = 24 grid, there are 7 member types, and for the N = 96 grid, there are 26.
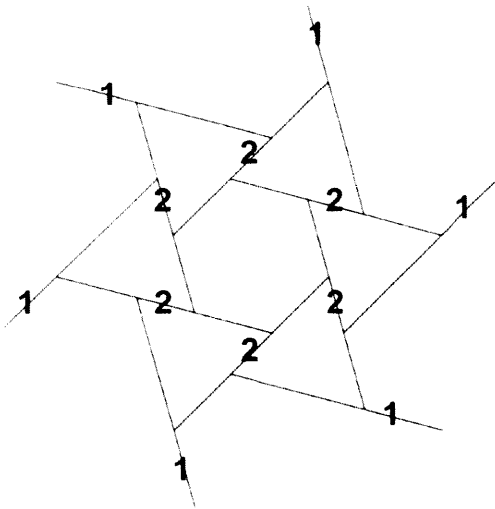
Figure 3-17 - Member types in an N = 6 Grid.   *Figure 3-18 - Member types in an N = 24 Grid.*
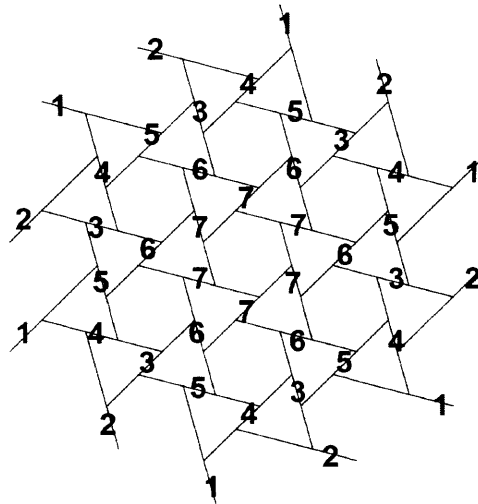
Under symmetric loading, the value of maximum moment for each member type is the same, with the centermost member types receiving the highest values of maximum moment. This may be counterintuitive as one may expect the outermost members to have the highest maximum moments, since it would "accumulate" all the loads from the center and bring it to the supports. However, the behavior of the entire grid can be thought of as a simply supported beam, with the highest moments at the midspan.

Taking an example from the N = 24 grid, the distribution of the 7 member types is shown in Figure 3-18. Type 7 is supporting types 7 and 6; type 6 is supporting 7 and 4; type 5 is supporting 6 and 1; type 4 is supporting 5 and 3; type 3 is supporting 5 and 2; type 2 is only supporting type 4; and type 1 is supporting only type 3. If you trace from type 7 the members that each are supporting, it is observed that the outer member types receive less load because they are supporting

members that carry less load. Due to symmetry, a majority of members have identical tributary areas and are supporting two members each, with the exception of the outermost members connected to the support points (type 1 and 2) – they are only supporting one member and have a different tributary area. As a consequence, members that support member type 1 and 2 (types 3 and 5) would subsequently receive less load than those further away from the outside, and in that sense the "accumulation" of loads is actually reversed in the case of an RF grid.

The ability to categorize members based on their loading distribution can be beneficial in terms of generating material savings, as the member size can be optimized based on their expected maximum load under symmetric and asymmetric loading.

3.9. Hand Calculation Verification

To verify the structural analysis results generated by the Karamba plugin, a hand calculation using Excel is performed (Microsoft 2016). As we are only interested in verifying the accuracy of the numerical results generated by the software, the simplest N = 6 grid with the uniform area load (neglecting self-weight) is chosen as the case to verify against. The values that are verified against the computer model are the Strain Energy Factor, and the values of maximum moment and shear. Since the N = 6 grid only has two member types (refer to Figure 3-17), only two members need to be analyzed in Excel as the remaining members would be identical in behavior to one of the two.

The first step is to import from Grasshopper the tributary areas for each node on the two members. The magnitude of the force on each node is then calculated by multiplying the areas by the applied area load. Type 1 members have 3 unknown forces, and type 2 members have 4 unknown forces (see Figure 3-19). The type 1 member is analyzed first as it is statically determinate: one of the unknowns is the reaction force (A_y), which can be solved due to symmetry (each reaction is equal to the total vertical force on the grid divided by the six supports). Therefore, two equations of equilibrium can be used to solve for all the remaining forces; sum of moments about point B to solve for C_y (Equation 5), and sum of vertical forces to solve for B_y (Equation 6).

$$C_y = -\frac{\sum(Applied\ Loads * Moment\ Arms\ to\ B) - (A_y * Length\ AB)}{Length\ BC} \tag{5}$$

$$B_y = -\left(A_y + C_y - \sum Applied\ Loads\right) \tag{6}$$
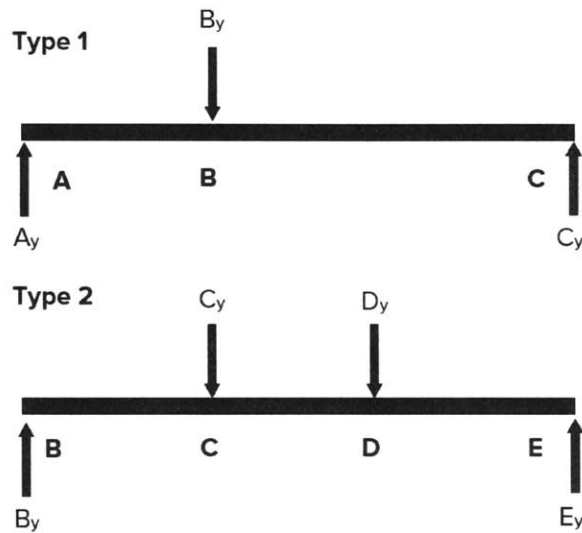
Figure 3-19 - Unknown forces on the two member types.
The known applied loads along the members are not shown for clarity.

Due to symmetry, the magnitude of the unknown C_y in member type 1 is equal to C_y in member type 2: this reduces the unknowns in member type 2 to two (D_y, E_y) and enables us to solve for the forces in a similar manner using Equations 7 and 8. After all the unknown forces are resolved, the shear and moment values at each node can be calculated. The moment values are then used to calculate the Strain Energy Factor in each member type, using Equation 2.

$$E_y = -\frac{\sum(Applied\ Loads * Moment\ Arms\ to\ D) + (C_y * Length\ CD) - (B_y * Length\ BD)}{Length\ DE} \tag{7}$$

$$D_y = -\left(B_y - C_y + E_y - \sum Applied\ Loads\right) \tag{8}$$

The results of the hand calculation are compared with the Karamba output in Table 3-5. Since the difference in the comparison values remain under 10%, the numerical results produced through the parameterized model can therefore be accepted with confidence. Refer to Appendix A for the spreadsheet of the hand calculations.

	Hand Calculation	Karamba Analysis	Difference
$\Sigma M_{max}{}^2$ [kNm^2]	2.17 x 10^6	2.30 x 10^6	-6.18%
Maximum Moment [kNm]	106	110	-3.11%
Maximum Shear [kN]	67.5	68.2	-1.10%

Table 3-5 - Comparison of hand calculation with Karamba output.

41

3.10. Summary of Methodology

The methodology of creating the parameterized structural analysis models was first discussed. The parameterization used Grasshopper, Karamba, and Rhino (Robert McNeel & Associates 2016, Preisinger 2016). The first step was to initialize the unit RF, from which we generated the three respective grid densities through a succession of polar arrays. The grids were then scaled to the appropriate size in order to maintain a constant surface area. Next, the procedure detailing how the member loads have been distributed based on tributary areas was described; this distribution of loads is a key contribution of this thesis to the research of planar reciprocal frames and their behavior under various load cases. The rationale behind the member sizing was discussed, and the Strain Energy Factor was introduced as the metric of structural performance for each geometry. Finally, a method of categorizing the members in an RF grid based on their load distribution and topology was presented. The methodology section concluded with a hand calculation procedure that was performed to verify the credibility of the Karamba analysis results.

4. Results

The general trend across all grid densities and load cases is that the more structurally efficient grids are those with a smaller rotation angle, and therefore larger engagement length. A common pattern is that the Strain Energy Factor initially decreases to a minimum at a rotation angle between 4 and 9 degrees, then increases for rotation angles beyond. Recall from Section 3.7 that a lower value for the Strain Energy Factor corresponds to a greater efficiency. The exact value of rotation angle at which the optimal structural performance exists varies between the different grid densities and load cases.

It is important to note that the results from the structural analysis are based on several assumptions. Buckling out of plane due to bending, and the effect of stress concentrations at the joints due to the assumed notching of members are not considered. Since certain rotation angles have joints that are closer together, the stress concentrations at these areas could have an effect on the efficiency of the structure that is not captured in the strain energy.

4.1. Organization of Results Section

The first part of the results section discusses the removal of certain data points due to possible errors from the structural analysis. The remaining sections summarize the analysis outputs, which have been organized in two ways: first, by grid density (Sections 4.3 to 4.5), which enables the comparison of results between load cases for a given density; and second by load case (Sections 4.6 to 4.9), which enables the comparison of results between grid densities for each load case. Primary discussion of the results are included in Sections 4.3 to 4.5 under each grid density. All presented graphs are scatter plots of the data points at each rotation angle. The results section closes with a comparison of a particular RF grid geometry with a similar non-reciprocal grid.

4.2. Filtering of Results

Upon reviewing the data points across the possible range of rotation angles, results from certain rotation angles were removed due to possible errors in the structural analysis.

The first errors are manifested through the member utilization: at small rotation angles for the N = 6 grid, the maximum member utilization would jump to values beyond 1.0, with many at 3000 – despite the fact that the value of maximum moment for those angles are less than those at

43

a higher, less optimal rotation angle. Although the bending moments corresponding to these erroneous utilization values appear to correlate with the trend of the moment values, these results are omitted due to possible errors. A similar problem occurs at the upper limit of rotation angles. In general, the glitch is not present between the rotation angles of 2 and 28 degrees. It is plausible that extremely high (and obviously erroneous) shear values may be contributing to the errors, even though the maximum shear utilization output by Karamba is still less than that of the bending utilization.

The second group of errors are from the grids with removed nodes. Recalling Section 3.3, certain rotation angles required the removal of closely spaced nodes in order to avoid problems with the Voronoi diagrams. However, it is found that this removal of nodes adversely affects the results, as it leads to a sharp decrease in the Strain Energy Factor, which does not follow the general pattern. Strain Energy Factors from rotation angles before and after those that have removed nodes correlate with the trend, which suggests that the values with the removed nodes cannot be trusted. These results are therefore removed from the results.

Depending on the grid density, the locations where results have been removed vary. Since the removed results represent a small portion of the total number of results, it is justified as it does not significantly affect the results.

4.3. N = 6 Grid Results

Key analysis outputs of the optimal rotation angle for the four load cases are tabulated in Table 4-1. The Strain Energy Factor for each rotation angle is plotted in Figure 4-1. The geometry at the optimal angles of 8.2 and 6.4 are shown in Figure 4-2.

At Optimal:	LC 1	LC 2	LC 3	LC 4
Rotation Angle [Deg.]	8.2	8.2	8.2	6.4
ΣM_{max}^2 [kNm^2]	2.67 x 10^6	2.91 x 10^6	1.27 x 10^6	8.69 x 10^5
Engagement Ratio	0.82	0.82	0.82	0.86
Maximum Moment [kNm]	111	118	115	72.9
Deflection Ratio	L/364	L/347	L/353	L/607

Table 4-1 - Analysis outputs of the optimal angle for each load case in the N = 6 Grid.

Figure 4-1 - Structural performance vs. rotation angle of all load cases for the N = 6 Grid.

Rotation Angle: 8.2°
Engagement Ratio: 0.82

Rotation Angle: 6.4°
Engagement Ratio: 0.86

Figure 4-2 - Optimal geometries for the N = 6 Grid.

4.3.1. Variation of Maximum Moments for N = 6 Grid

Figure 4-3 shows the value of maximum moments at each rotation angle for the two member types under symmetric loading (load case 1). Figure 4-4 shows the member type maximum moments under the most asymmetric loading (load case 4).

Maximum Moments for LC 1 (N = 6 Grid)

Figure 4-3 - LC 1 maximum moments for each member type in the N = 6 Grid.

Maximum Moments for LC 4 (N = 6 Grid)

Figure 4-4 - LC 4 maximum moments for each member type in the N = 6 Grid.

4.3.2. Discussion of Results for N = 6 Grid

The results show that the change in structural performance over rotation angles remains relatively consistent for both symmetric and asymmetric load cases; the higher the rotation angle, the less efficient the geometry. Beyond a rotation angle of approximately 19 degrees, the structural performance flattens out, which suggests that there is little compromise in efficiency between those rotation angles. The structural performance generally follows the same curve as the value of global maximum moment in the grid, which in this case is of member type 2. The optimal geometry does not lie at an extremity of the range of rotation angles, but rather at a minimum at 8.2 degrees for load case 1-3 and 6.4 degrees for load case 4.

Since load case 1 and 2 are both symmetric load cases, it was expected that their optimal geometries would remain similar. However, even under asymmetric loading in load case 3, the optimal angle remained the same. With load case 4 being the most asymmetric load case, it was anticipated that the optimal rotation angle would be very different. However, the difference in only 1.8 degrees show that asymmetric loading has little impact on the efficiency of the grid geometry.

In terms of maximum moments, it is observed that the trend of the moments remains the same for both symmetric and asymmetric load cases, except in the asymmetric load case the difference in moments between type 1 and type 2 is decreased. Note in both graphs that the optimal rotation angle does not lie at the location of smallest maximum moment (type 2 minimum).

It is observed that the global maximum moment continues to increase up to a rotation angle of 19.1 degrees, before decreasing slightly and then increasing again. This is due to the location of the connecting members for a given rotation angle: as the rotation angle approaches 19.1 degrees, the point at which a member is supporting another moves towards the center of the beam, which translates to a larger lever arm for the moment. After 19.1 degrees, the two connection points for a given interior member crossover, switch respective locations, and begin to move closer to the supports again.

However, despite the lever arm being reduced as the rotation angle continues to increase beyond 19.1 degrees, the value of maximum moment is seen to increase again towards the upper end of rotation angles. This is likely because the total tributary area of the nodes along the central

span are larger, therefore increasing the magnitude of the applied loads along the center of the beam.

4.4. N = 24 Grid Results

Key analysis outputs of the optimal rotation angle for the four load cases are tabulated in Table 4-2. The Strain Energy Factor for each rotation angle is plotted in Figure 4-5. The geometry at the optimal angles of 4.2 and 4.0 degrees is shown in Figure 4-6.

At Optimal:	LC 1	LC 2	LC 3	LC 4
Rotation Angle [Deg.]	4.2	4.2	4.2	4.0
ΣM_{max}^2 [kNm^2]	1.20×10^6	1.31×10^6	1.27×10^6	4.40×10^5
Engagement Ratio	0.92	0.92	0.92	0.93
Maximum Moment [kNm]	56.1	61.1	57.8	37.5
Deflection Ratio	L/710	L/673	L/690	L/1176

Table 4-2 - Analysis outputs of the optimal angle for each load case in the N = 24 Grid.

48

Structural Performance vs. Rotation Angle (N = 24 Grid)
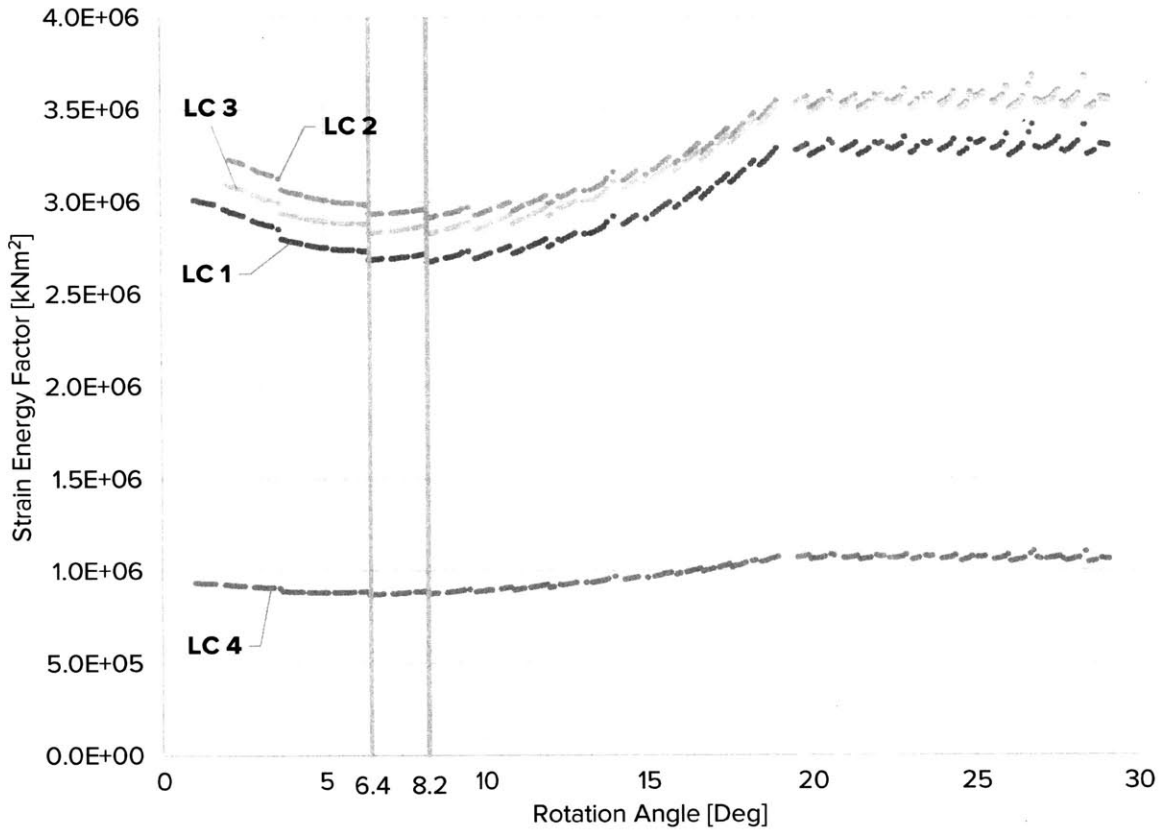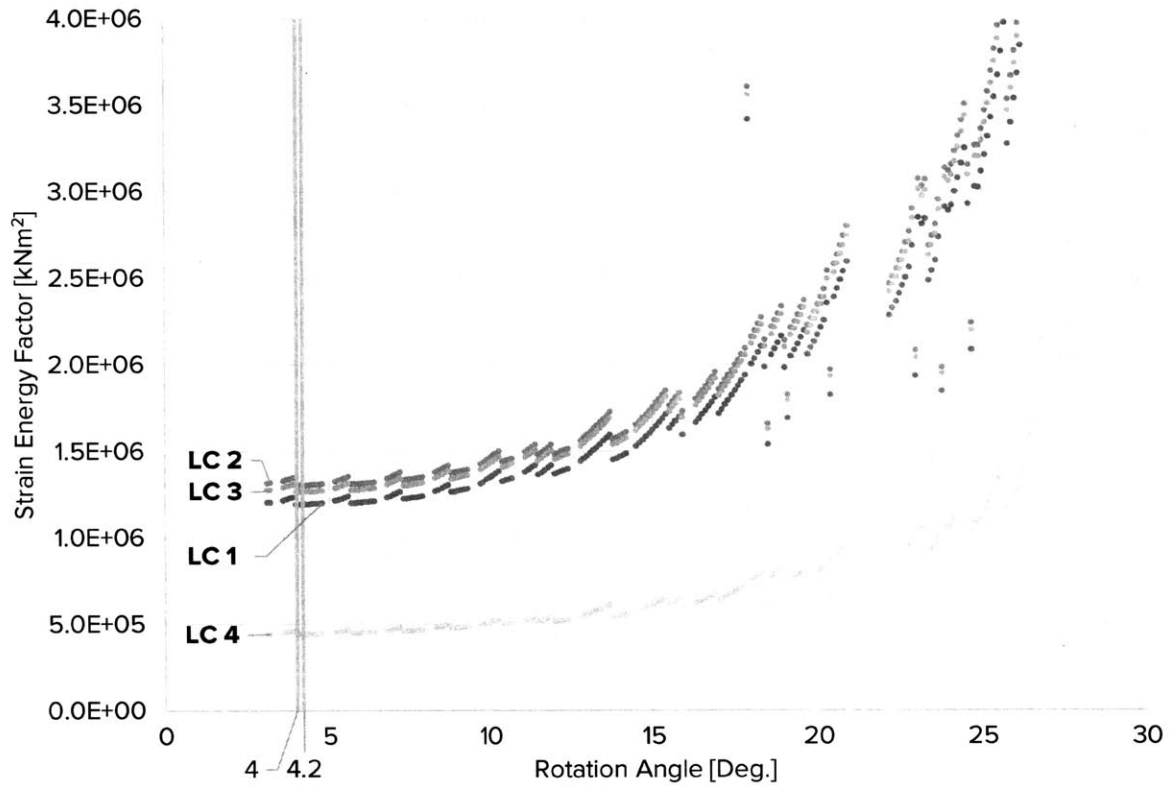
Figure 4-5 - Structural performance vs. rotation angle of all load cases for the N = 24 Grid.
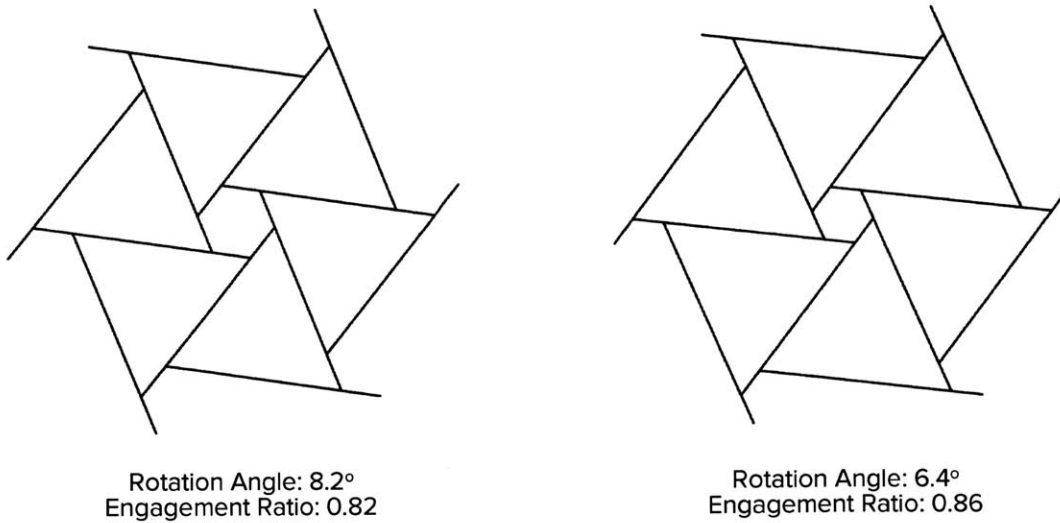

Rotation Angle: 4.2°
Engagement Ratio: 0.92

Rotation Angle: 4.0°
Engagement Ratio: 0.93
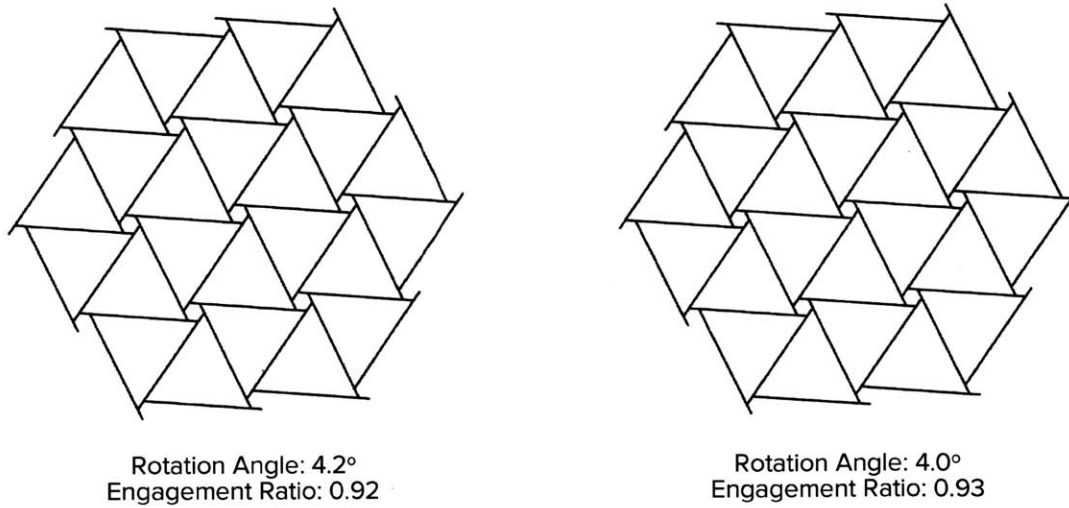
Figure 4-6 - Optimal geometries for the N = 24 Grid.

4.4.1. Variation of Maximum Moments for N = 24 Grid

Figure 4-7 shows the value of maximum moments at each rotation angle for the seven member types under symmetric loading (load case 1). Figure 4-8 shows the member type maximum moments under the most asymmetric loading (load case 4).
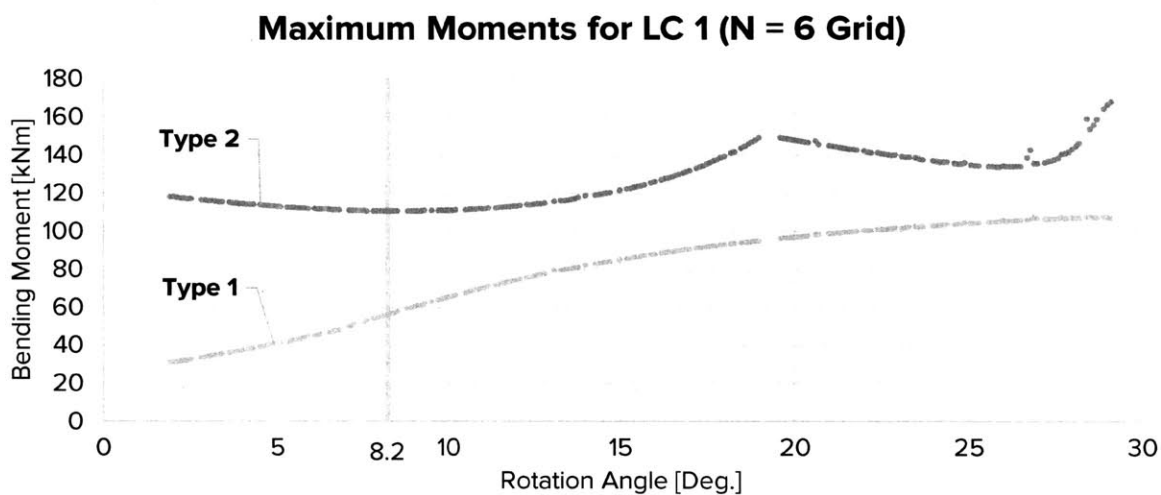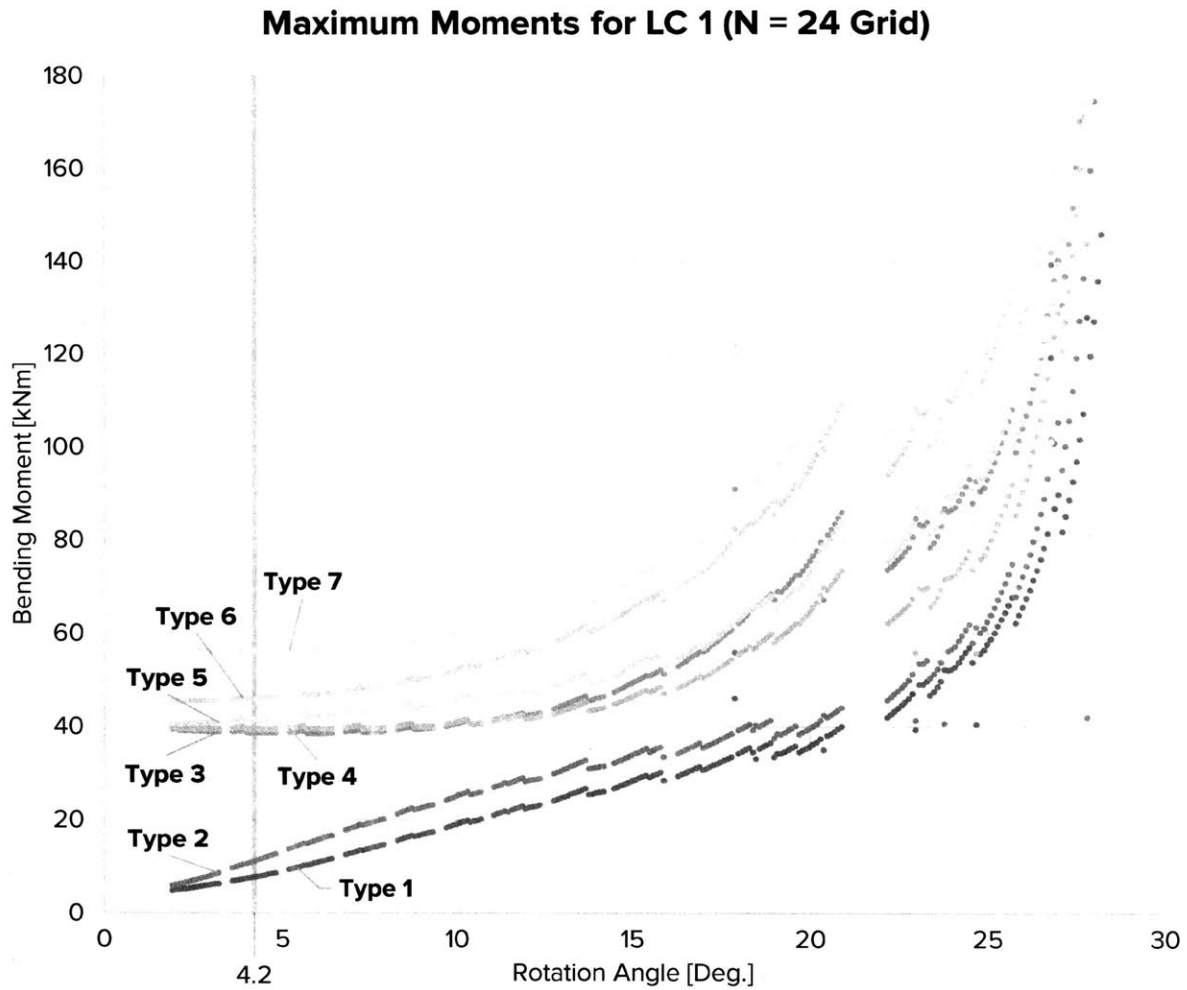

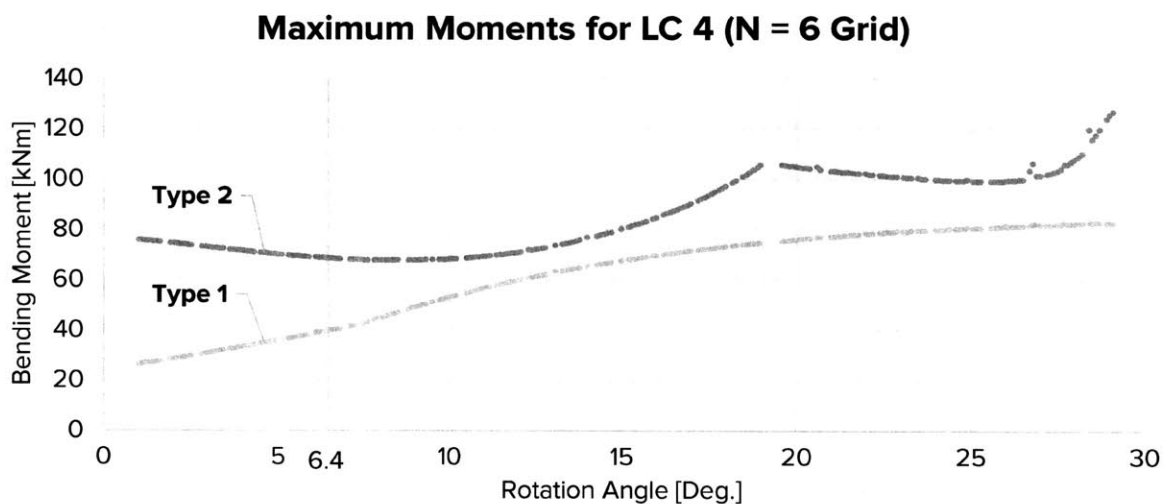*Figure 4-7 - LC 1 maximum moments for each member type in the N = 24 Grid.*
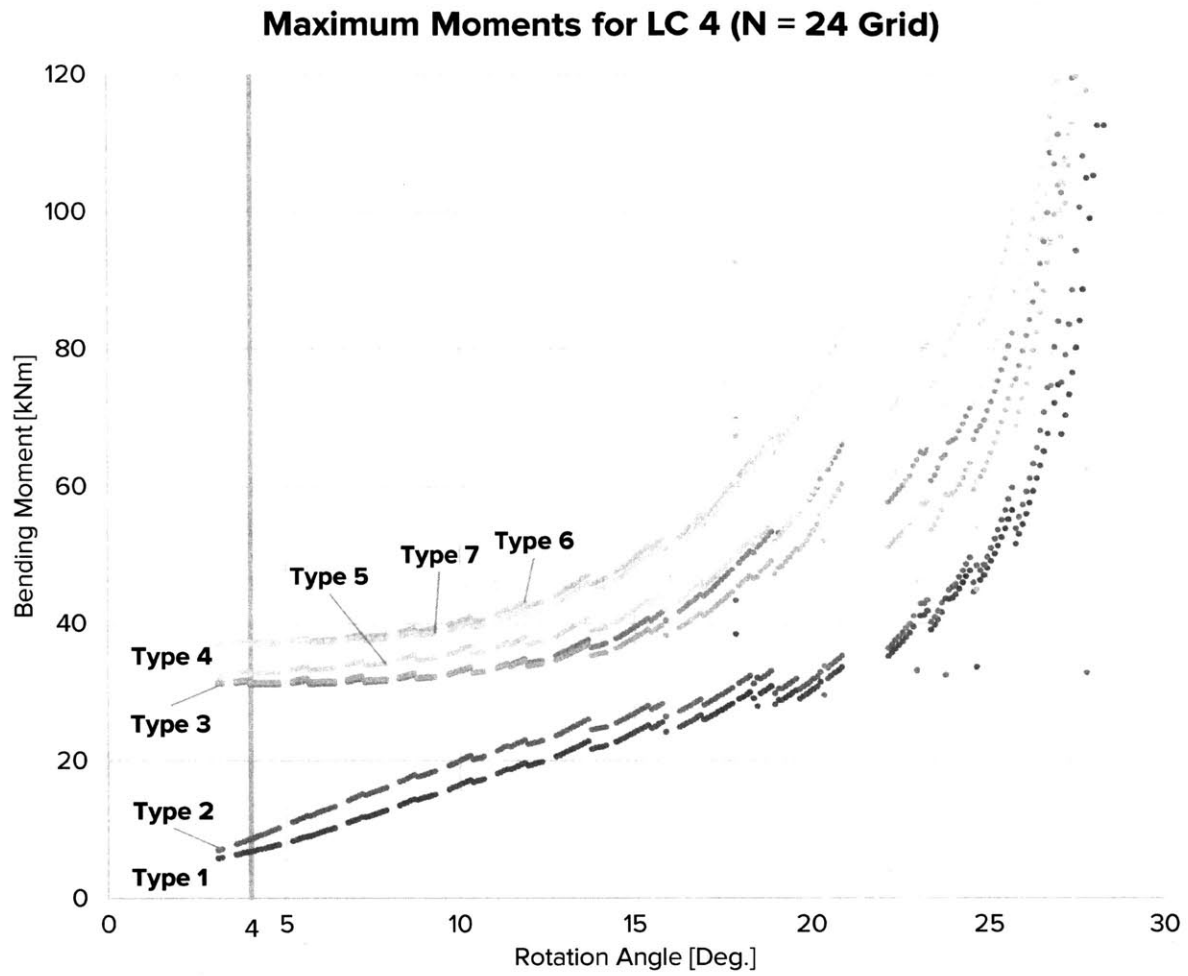
Figure 4-8 - LC 4 maximum moments for each member type in the N = 24 Grid.

4.4.2. Discussion of Results for N = 24 Grid

Similar to the N = 6 Grid, the optimal rotation angle does not lie at an extremity but at 4.2 or 4.0 degrees. Although the optimal rotation angle for load case 4 is 0.2 degrees off from the other 3 load cases, the relative difference in the Strain Energy Factor for 4.2 and 4.0 degrees is only 0.06% in load case 4, which can be considered negligible in terms of compromised efficiency. Note that the Strain Energy Factor is relatively flat for low rotation angles up to about 7 degrees; this correlates with the small difference in values between 4.2 and 4.0 degrees, and suggests that this range of rotation angles all produce similarly efficient geometries.

Similar to the N = 6 grid results, the maximum moment and structural performance graphs are closely correlated. However, the shapes of the graphs are dramatically different from the N = 6 grid: although a minimum is still found at a rotation angle that is not the smallest possible, the values increase at a much more rapid rate as the rotation angle increases, in contrast with the N = 6 grid where the values flatten out after about 19 degrees.

In terms of member type maximum moments, the trend is similar to the N = 6 grid in the sense that an asymmetric loading case brings the moment values between members in closer proximity. The member types also appear to be grouped according to their maximum moments: types 1 and 2 are close to one another; types 3, 4 and 5 are close to one another; and types 6 and 7 are close to one another. This makes sense when we revisit Section 3.8 and note the relative locations of the member types radially from the center. An interesting observation is the crossing over of maximum moments between certain member types: for example, the maximum moment of member type 3 crosses over member type 4 at about 12.5 degrees. Finally, in line with the structural performance graph, the graph of maximum moments is relatively flat for member types 3 to 7 for low rotation angles.

4.5.   N = 96 Grid Results

Key analysis outputs of the optimal rotation angle for the four load cases are tabulated in Table 4-3. The Strain Energy Factor for each rotation angle is plotted in Figure 4-9. The geometry at the optimal angles of 4.1 degrees is shown in Figure 4-10.

At Optimal:	LC 1	LC 2	LC 3	LC 4
Rotation Angle [Deg.]	4.1	4.1	4.1	4.1
ΣM_{max}^2 [kNm^2]	6.32 x 10^5	6.82 x 10^5	6.73 x 10^5	2.37 x 10^5
Engagement Ratio	0.91	0.91	0.91	0.91
Maximum Moment [kNm]	28.5	31.9	29.4	19.6
Deflection Ratio	L/248	L/207	L/240	L/414

Table 4-3 - Analysis outputs of the optimal angle for each load case in the N = 96 Grid.
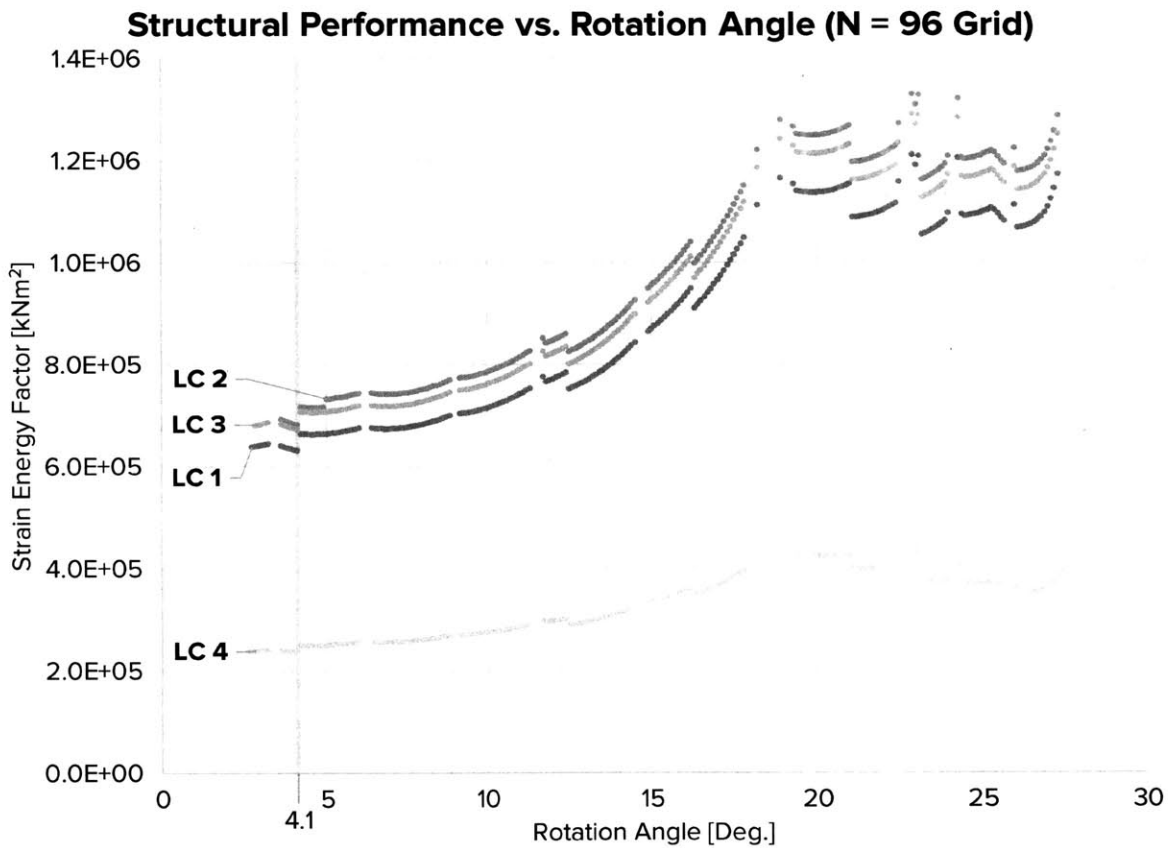
Figure 4-9 - Structural performance vs. rotation angle of all load cases for the N = 96 Grid.
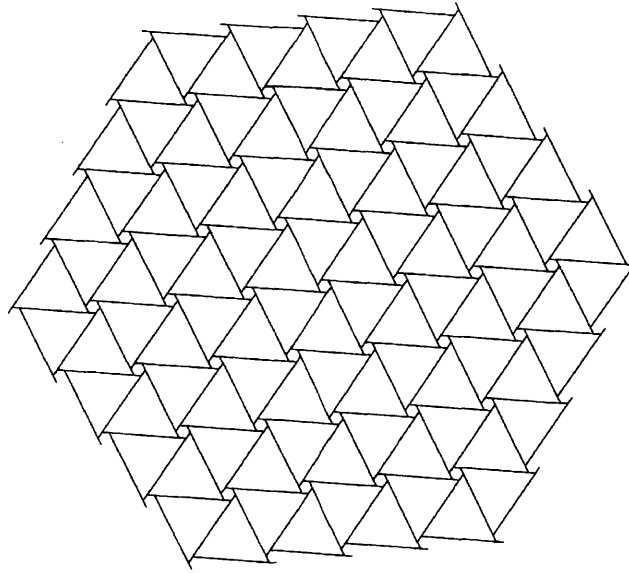
Rotation Angle: 4.1°
Engagement Ratio: 0.91

Figure 4-10 - Optimal geometry for the N = 96 Grid.

4.5.1. Variation of Maximum Moments for N = 96 Grid

Figure 4-11 shows the value of maximum moments at each rotation angle for the twenty-six member types under symmetric loading (load case 1). Figure 4-12 shows the member type maximum moments under the most asymmetric loading (load case 4).

Maximum Moments for LC 1 (N = 96 Grid)
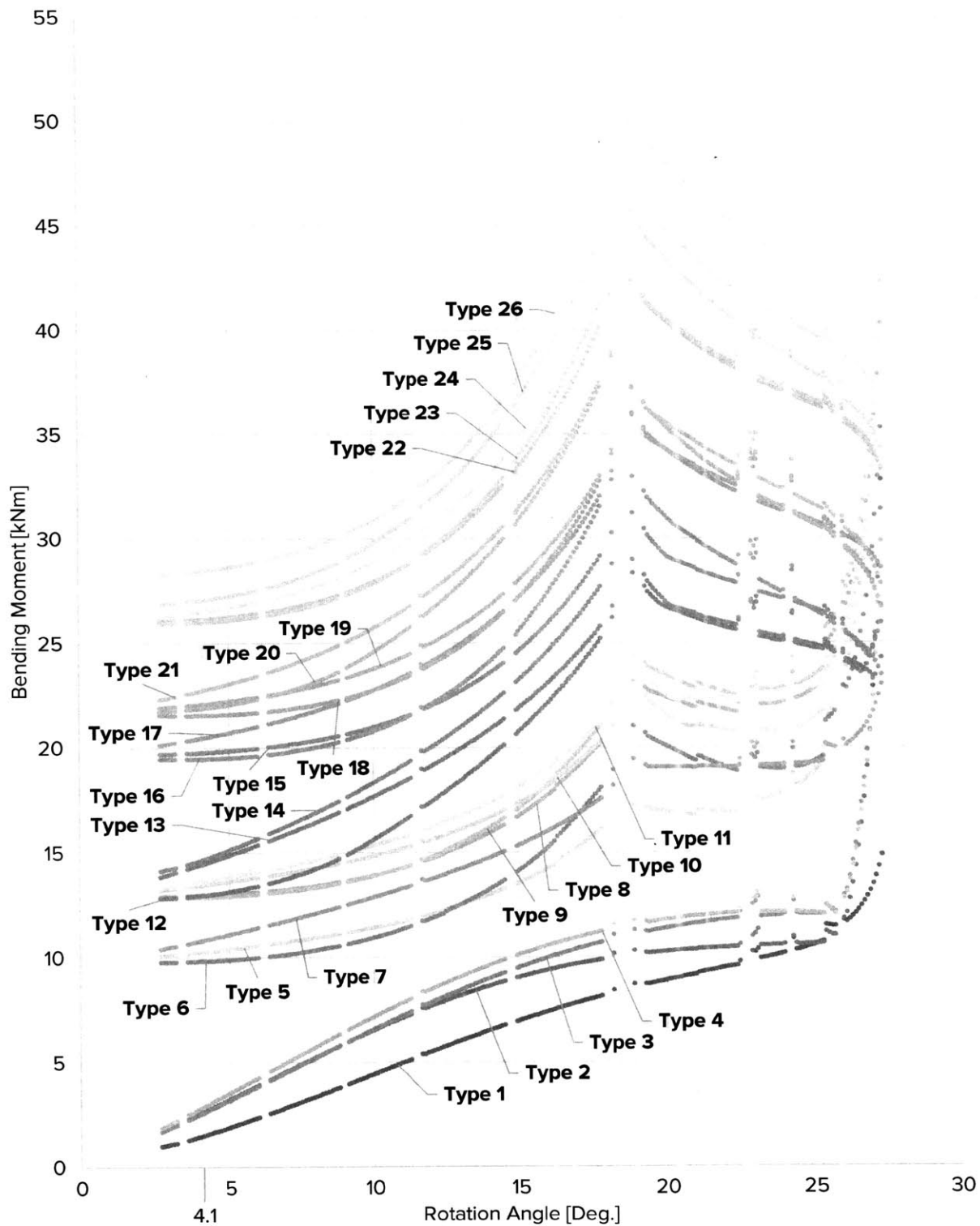
Figure 4-11 - LC 1 maximum moments for each member type in the N = 96 Grid.

Figure 4-12 - LC 4 maximum moments for each member type in the N = 96 Grid.

4.5.2. Discussion of Results for N = 96 Grid

Similar to the two previous grid densities, the optimal rotation angle does not occur at an extremity but at 4.1 degrees, and in this case is the optimal for all load cases. In addition, the angle is very similar to that of the N = 24 optimal (4.2 degrees).

As expected, the structural performance and maximum moment graphs generally correlate. In addition, the graphs also appear to return to the likeliness of the N = 6 grid results: the Strain Energy Factor increases up to around 19 degrees, then flattens out. For the maximum moments, they increase up to 19 degrees, then decrease like the N = 6 grid. Furthermore, the curve of maximum moments in the type 1-4 members closely resembles that of the type 1 members in the N = 6 grid.

Finally, the maximum moments are also grouped in a similar manner like the N = 24 grid: types 1 to 4 are one group, followed by types 5 to 7; types 8 to 11; types 12 to 14; types 15 to 17; types 18 to 21; and types 22 to 26. The crossing over of maximum moments between member types is also evident in this grid density.

Based on the results for all grid densities, it can be concluded that the most efficient geometry for symmetric loading is also relatively efficient for asymmetric loading. The implications of this result is positive as it suggests that for a given RF grid structure with any particular geometry, it would not be performing in a greatly inefficient manner when subject to asymmetric loading.

4.6. Load Case 1 Results

The results are now presented according to load case, in order to compare the impact of grid density on the structural performance. Key analysis outputs in this load case for the optimal angle in the three grid densities are shown in Table 4-4.

At Optimal:	N = 6 Grid	N = 24 Grid	N = 96 Grid
Rotation Angle [Deg.]	8.2	4.2	4.1
ΣM_{max}^2 [kNm^2]	2.67 x 10^6	1.20 x 10^6	6.32 x 10^5
Engagement Ratio	0.82	0.92	0.91
Maximum Moment [kNm]	111	56.1	28.5
Deflection Ratio	L/364	L/710	L/248

Table 4-4 - Analysis outputs from the optimal geometry for Load Case 1.

The results suggest that denser grids are more efficient, as they have a lower Strain Energy Factor. This makes sense as the maximum bending moments in the members are reduced due to the shorter spans (shorter member lengths). Furthermore, the two denser grids appear to share a similar optimum, with a difference in optimal rotation angle of only 0.1 degrees. Despite having a lower overall strain energy, the deflections of the N = 96 grid appear to be larger. This is likely due to the fact that more members are involved in spanning across the grid, and therefore there is a greater accumulation of each individual member deflection.

The much lower deflection ratio for the N = 24 grid is likely due to the oversizing of the members for that particular geometry. As mentioned in Section 3.5 the members had to be sized for the least optimal bending moment in load case 2, and for the N = 24 case the bending moments increase dramatically with increasing rotation angle.

4.7. Load Case 2 Results

Key analysis outputs in this load case for the optimal angle in the three grid densities are shown in Table 4-5.

At Optimal:	N = 6 Grid	N = 24 Grid	N = 96 Grid
Rotation Angle [Deg.]	8.2	4.2	4.1
ΣM_{max}^2 [kNm^2]	2.91 x 10^6	1.31 x 10^6	6.82 x 10^5
Engagement Ratio	0.82	0.92	0.91
Maximum Moment [kNm]	118	61.1	31.9
Deflection Ratio	L/347	L/673	L/207

Table 4-5 - Analysis outputs from the optimal geometry for Load Case 2.

Note that for the N = 96 grid, the deflection ratio exceeds a typical deflection limit of L/240, which means that deflection would govern the sizing of the members for this grid density.

4.8. Load Case 3 Results

Key analysis outputs in this load case for the optimal angle in the three grid densities are shown in Table 4-6.

At Optimal:	N = 6 Grid	N = 24 Grid	N = 96 Grid
Rotation Angle [Deg.]	8.2	4.2	4.1
ΣM_{max}^2 [kNm^2]	1.27 x 10^6	1.27 x 10^6	6.73 x 10^5
Engagement Ratio	0.82	0.92	0.91
Maximum Moment [kNm]	115	57.8	29.4
Deflection Ratio	L/353	L/690	L/240

Table 4-6 - Analysis outputs from the optimal geometry for Load Case 3.

4.9. Load Case 4 Results

Key analysis outputs in this load case for the optimal angle in the three grid densities are shown in Table 4-7.

At Optimal:	N = 6 Grid	N = 24 Grid	N = 96 Grid
Rotation Angle [Deg.]	6.4	4.0	4.1
ΣM_{max}^2 [kNm^2]	8.69 x 10^5	4.40 x 10^5	2.37 x 10^5
Engagement Ratio	0.86	0.93	0.91
Maximum Moment [kNm]	72.9	37.5	19.6
Deflection Ratio	L/607	L/1176	L/414

Table 4-7 - Analysis outputs from the optimal geometry for Load Case 4.

4.10. Comparison with Non-Reciprocal Grid

To compare the structural performance of the RF grid with a conventional planar grid, the non-reciprocal N = 24 grid at a rotation angle of 19.1 degrees is compared with the N = 24 grid at 18.6 degrees. This was chosen to ensure a comparison between structural frames that remain similar in geometry, and to avoid an overlap of the members at the joints based on the assumed member width.

The key difference in a non-reciprocal grid is in the requirement of the members and connections: if pinned connections are desired, then long members spanning the entire span would be needed in one direction in order to support members in the other direction; otherwise, moment connections would be required for all the joints between short members, which could be impractical. Alternatively, all moment connections could also be used in the long member case. The comparison will use the case where all the short members are moment connected with each other. The member cross-sections and material properties are the same as described for the N = 24 grid in Section 3.5, and load case 1 is used.
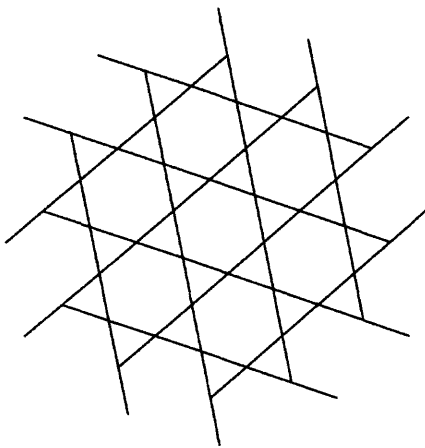
Figure 4-13 - Example of a non-reciprocal grid with geometry similar to an RF grid.
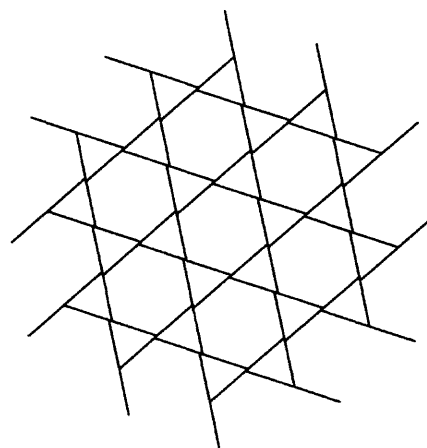
Figure 4-14 - RF Grid at a rotation angle of 18.6 degrees.

	RF Grid	Non-Reciprocal Grid
ΣM_{max}^2 [kNm²]	2.05 x 10⁶	1.20 x 10⁶
Maximum Moment [kNm]	92.9	64.3
Deflection Ratio	L/482	L/1041

Table 4-8 - Comparison of analysis outputs between an RF Grid and Non-RF Grid.

The Strain Energy Factor for the non-reciprocal grid is lower than that of the RF grid, which means that the non-reciprocal grid is more efficient according to our definition. This finding correlates with the comparison performed by Gelez et al. (2011), between an RF grid of rectangular topology and a conventional grid: the RF grid is not able to compete in terms of maximum bending moment and deflection, and therefore has more total strain energy. However as noted in the literature review, an RF grid remains advantageous in terms of robustness achieved through redundancy, constructability through the use of shorter members and simple pin connections, and adaptability to irregular perimeters.

5. Conclusion

The results from this thesis complement the relatively small body of work that has been done in investigating the structural efficiency of reciprocal frame structures. With many possible geometries for a given topology of a reciprocal frame structure, few studies have been conducted on whether an optimal geometry exists for multiple load cases. Furthermore, despite offering architectural, structural, and constructability benefits, researchers have noted that built examples of reciprocal frame structures continue to be rare as much of their structural behavior remains to be understood (Parigi and Kirkegaard 2013a). By exploring how the efficiency of an RF grid changes with geometry, this thesis furthers the understanding of how the structural behavior of an RF is impacted by geometry.

Building on past research performed by Parigi & Kirkegaard (2013a), this thesis models the behavior of a planar reciprocal frame with triangular topology as a hypothetical roof or floor framing structure, by taking into account the distribution of gravity load by tributary areas. This is in contrast with all past research on the structural behavior of RF grids, where all members receive identical uniform loading. Furthermore, the metric of structural performance in this thesis was derived from the global strain energy, which better portrays the efficiency of a reciprocal frame as a whole.

The results show that for a given grid density, the optimal geometry for the symmetric load case does not lie far from the asymmetric load case. The optimal rotation angle of the $N = 6$ grid for all load cases is 8.2 degrees, with the exception of load case 4 (the most asymmetrical load case), where it is 6.4 degrees. The optimal angle of the $N = 24$ grid is 4.2 degrees, with the exception of load case 4 where it is 4.0 degrees. The optimal angle of the $N = 96$ grid is 4.1 degrees for all load cases. The optimum geometry of each grid density for load case 1 (a symmetric load case) is shown Figure 5-1. As a general rule of thumb, the efficiency of a planar RF grid decreases as the rotation angle increases (or as the engagement ratio decreases), and increases as the grid density increases.

N = 6 Grid	N = 24 Grid	N = 96 Grid
Rotation Angle: 8.2°	Rotation Angle: 4.2°	Rotation Angle: 4.1°
Engagement Ratio: 0.82	Engagement Ratio: 0.92	Engagement Ratio: 0.91
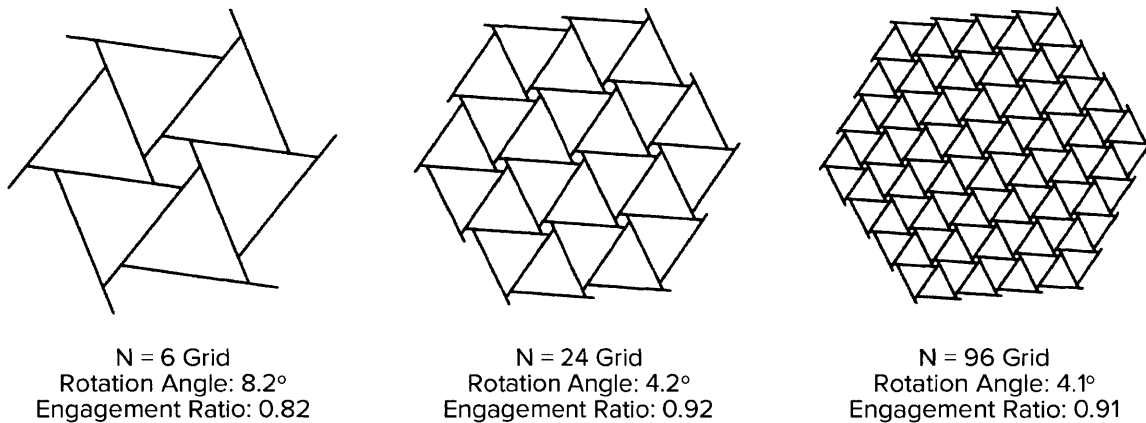
Figure 5-1 - Optimal geometries for load case 1.

The results are promising as they suggest that planar RF structures are a good fit for cases where asymmetric loading may occur frequently, since their geometric configuration would not be much less efficient than if it was loaded symmetrically. Given that asymmetric loading often occurs for a floor or roof framing structure, the results suggest that a planar RF structure is a good fit for that application.

5.1. Future Work

Potential for future work includes expanding the research to additional RF topologies. For topologies where the geometry cannot be described in terms of a rotation angle (for instance the rectangular topology), the size of the engagement window can be used to compare results between different topologies. It would be valuable to determine whether the structural performance of the rectangular topology decreases as the engagement window becomes smaller, and whether the most efficient geometry under symmetric loading would also be close to the efficient geometry for asymmetrical loading.

Another area of interest for further development is in the optimization of members based on their member type, as mentioned in Section 3.8. It would be interesting to evaluate the material savings that can be realized if each member type was optimized for their expected maximum loading under both symmetric and asymmetric load cases.

64

6. References

American Society of Civil Engineers. 2013. Minimum Design Loads for Buildings and Other Structures. In *ASCE 7-10*. Reston, Virginia: American Society of Civil Engineers.

Baverel, O. 2004. "Configuration Processing of Nexorades using Genetic Algorithms." *Journal of the International Association for Shell and Spatial Structures* 45:99-108.

European Committee for Standardization. 2003. Structural timber - Strength classes (EN 338).

Gelez, Simon, Simon Aubry, and Bernard Vaudeville. 2011. "Behavior of a Simple Nexorade or Reciprocal Frame System." *International Journal of Space Structures* 26 (4):331-342.

Kaethner, S.C., and J.A. Burridge. 2012. "Embodied CO2 of structural frames." *The Structural Engineer* 90 (5):33-40.

Kingsford, Ed. KREOD / Chun Qing Li of Pavilion Architecture.

Kirkegaard, Poul Henning, and Dario Parigi. 2013b. "Robustness Analysis of Typologies of Reciprocal Timber Structures." International Association for Shell and Spatial Structures Symposium, Poland.

Kohlhammer, Thomas, and Toni Kotnik. 2011. "Systemic Behaviour of Plane Reciprocal Frame Structures." *Structural Engineering International* 21 (1):80-86. doi: 10.2749/101686611x12910257102596.

Larsen, O. P. 2014. "Reciprocal Frame (RF) Structures: Real and Exploratory." *Nexus Network Journal* 16 (1):119-134. doi: 10.1007/s00004-014-0181-0.

Larsen, Olga Popovic. 2008. *Reciprocal Frame Architecture*. Oxford, UK: Elsevier.

Larsen, Olga Popovic, and Daniel Sang-Hoon Lee. 2013. "Reciprocal Frames (RFs) Used for Quick-built Deployable Emergency Shelters." International Association for Shell and Spatial Structures (IASS) Symposium, Poland.

Microsoft Excel 2016. Microsoft.

Parigi, Dario, and Poul Henning Kirkegaard. 2013a. "Structural Behaviour of Reciprocal Structures." International Association for Shell and Spatial Structures (IASS) Symposium, Poland.

Preisinger, Clemens. Karamba 1.1.0.

Robert McNeel & Associates. GhPython 0.6.0.3.

Robert McNeel & Associates. Grasshopper 0.9.0076.

Robert McNeel & Associates. Rhinoceros Version 5 SR12.

Appendix A

This appendix contains the spreadsheet of the hand calculation verification discussed in Section 3.9. The equations used to solve for the unknown forces shaded in light grey are found in Section 3.9. The shear force at a node is calculated from summing the shear force at the previous node with the applied force on the node. "dM" represents the change in bending moment between two nodes, which is calculated from the area of the shear diagram between two nodes. The value of moment at a given node is therefore the sum of the moment at the previous node and the change in moment (dM).

HAND CALCULATION VERIFICATION									
Global Parameters									
Rotation Angle [Deg.]	15		E [kN/m^2]		1.05E+07				
Area Load [kPa]	-4.8		b [in]		6.00		b [m]		1.52E-01
			h [in]		28.00		ħ [m]		7.11E-01
							I [m^4]		4.57E-03

*Positive force indicates upwards force; positive moment indicates counterclockwise moment.

Member 11 (Type 1)	Node ID	Trib. Area [m^2]	Force [kN]	Dist. from A [m]	Moment about B [kNm]	Shear [kN]	dM	Moment [kNm]	M^2
Ay	841		47	0	-79.9000	47.00			
A	841	2.297461	0	0	0.0000	47.00		0.00	0.00
	842	0.012734	-0.06112	0.1	0.0978	46.94	4.70	4.70	22.09
	843	0.025469	-0.12225	0.2	0.1834	46.82	4.69	9.39	88.25
	844	0.038204	-0.18338	0.3	0.2567	46.63	4.68	14.08	198.12
	845	0.050939	-0.24451	0.4	0.3179	46.39	4.66	18.74	351.15
	846	0.063674	-0.30564	0.5	0.3668	46.08	4.64	23.38	546.52
	847	0.076409	-0.36676	0.6	0.4034	45.72	4.61	27.99	783.22
	848	0.089144	-0.42789	0.7	0.4279	45.29	4.57	32.56	1060.00
	849	0.101879	-0.48902	0.8	0.4401	44.80	4.53	37.09	1375.41
	850	0.114618	-0.55017	0.9	0.4401	44.25	4.48	41.57	1727.77
	851	0.127349	-0.61128	1	0.4279	43.64	4.42	45.99	2115.21
	852	0.134043	-0.64341	1.1	0.3860	42.99	4.36	50.36	2535.65
	853	0.120875	-0.5802	1.2	0.2901	42.41	4.30	54.65	2987.13
	854	0.106182	-0.50967	1.3	0.2039	41.90	4.24	58.90	3468.75
	855	0.091489	-0.43915	1.4	0.1317	41.47	4.19	63.09	3979.92
	856	0.07679	-0.36859	1.5	0.0737	41.10	4.15	67.23	4520.29
	857	0.057673	-0.27683	1.6	0.0277	40.82	4.11	71.34	5089.80
By	324		-58.2018	1.7	0.0000	-17.38	4.08	75.42	
B	324	0.028092	-0.13484	1.7	0.0000	-17.52	0.00	75.42	5688.91
	858	0.032085	-0.15401	1.72	-0.0031	-17.67	-0.35	75.07	5636.18
	859	0.060075	-0.28836	1.82	-0.0346	-17.96	-1.77	73.31	5373.98
	860	0.068926	-0.33084	1.92	-0.0728	-18.29	-1.80	71.51	5113.90
	861	0.077769	-0.37329	2.02	-0.1195	-18.66	-1.83	69.68	4855.66
	862	0.086611	-0.41573	2.12	-0.1746	-19.08	-1.87	67.82	4599.05
	863	0.095453	-0.45817	2.22	-0.2383	-19.54	-1.91	65.91	4343.92
	864	0.104294	-0.50061	2.32	-0.3104	-20.04	-1.95	63.95	4090.21
	865	0.113136	-0.54305	2.42	-0.3910	-20.58	-2.00	61.95	3837.92
	866	0.121978	-0.58549	2.52	-0.4801	-21.17	-2.06	59.89	3587.16
	867	0.130819	-0.62793	2.62	-0.5777	-21.79	-2.12	57.78	3338.10
	868	0.139661	-0.67037	2.72	-0.6838	-22.46	-2.18	55.60	3091.01
	869	0.148503	-0.71281	2.82	-0.7984	-23.18	-2.25	53.35	2846.27
	870	0.157344	-0.75525	2.92	-0.9214	-23.93	-2.32	51.03	2604.34
	871	0.166186	-0.79769	3.02	-1.0530	-24.73	-2.39	48.64	2365.80
	872	0.174988	-0.83994	3.12	-1.1927	-25.57	-2.47	46.17	2131.34
	873	0.177028	-0.84973	3.22	-1.2916	-26.42	-2.56	43.61	1901.78
	874	0.174091	-0.83564	3.32	-1.3537	-27.26	-2.64	40.97	1678.33
	875	0.171172	-0.82163	3.42	-1.4132	-28.08	-2.73	38.24	1462.44
	876	0.168251	-0.8076	3.52	-1.4698	-28.88	-2.81	35.43	1255.58
	877	0.165326	-0.79356	3.62	-1.5236	-29.68	-2.89	32.55	1059.22
	878	0.1624	-0.77952	3.72	-1.5746	-30.46	-2.97	29.58	874.85
	879	0.159475	-0.76548	3.82	-1.6228	-31.22	-3.05	26.53	703.95
	880	0.156435	-0.75089	3.92	-1.6670	-31.97	-3.12	23.41	548.02
	881	0.141204	-0.67778	4.02	-1.5724	-32.65	-3.20	20.21	408.54
	882	0.11767	-0.56482	4.12	-1.3669	-33.22	-3.27	16.95	287.21
	883	0.094135	-0.45185	4.22	-1.1387	-33.67	-3.32	13.63	185.65
	884	0.0706	-0.33888	4.32	-0.8879	-34.01	-3.37	10.26	105.24
	885	0.04706	-0.22589	4.42	-0.6144	-34.23	-3.40	6.86	47.03
	886	0.023372	-0.11219	4.52	-0.3164	-34.35	-3.42	3.43	11.80
C	887	0.040216	-0.19304	4.62	-0.5637	-34.54	-3.43	0.00	0.00
Cy	887		34.5386	4.62	100.8527	0.00	0.00	0.00	0.00
		SUM	0	SUM	0.0000			SUM	104883
								ΣM^2/(2EI)	1.0932

68

Member 0 (Type 2)	Node ID	Trib. Area [m²]	Force [kN]	Dist. from B [m]	Moment about D [kNm]	Shear [kN]	dM	Moment [kNm]	M²
By	324		58.2018	0	-171.1134	58.2018			
B	324	0.028092	-0.13484	0	0.3964	58.0670		0	0.00
	325	0.023372	-0.11219	0.1	0.3186	57.9548	5.81	5.81	33.72
	326	0.04706	-0.22589	0.2	0.6189	57.7289	5.80	11.60	134.61
	327	0.0706	-0.33888	0.3	0.8946	57.3900	5.77	17.38	301.89
	328	0.094135	-0.45185	0.4	1.1477	56.9382	5.74	23.11	534.26
	329	0.11767	-0.56482	0.5	1.3782	56.3734	5.69	28.81	829.89
	330	0.139294	-0.66861	0.6	1.5646	55.7048	5.64	34.45	1186.47
	331	0.149621	-0.71818	0.7	1.6087	54.9866	5.57	40.02	1601.26
	332	0.15801	-0.75845	0.8	1.6231	54.2281	5.50	45.51	2071.56
	333	0.1664	-0.79872	0.9	1.6294	53.4294	5.42	50.94	2594.60
	334	0.174089	-0.83563	1	1.6211	52.5938	5.34	56.28	3167.45
	335	0.167748	-0.80519	1.1	1.4816	51.7886	5.26	61.54	3787.11
	336	0.155981	-0.74871	1.2	1.3028	51.0399	5.18	66.72	4451.34
	337	0.144213	-0.69222	1.3	1.1352	50.3477	5.10	71.82	5158.45
	338	0.132445	-0.63574	1.4	0.9790	49.7119	5.03	76.86	5907.02
	339	0.115708	-0.5554	1.5	0.7998	49.1565	4.97	81.83	6695.87
	340	0.085668	-0.41121	1.6	0.5510	48.7453	4.92	86.74	7524.52
Cy	652		-34.5386	1.7	42.8279	14.2067	4.87	91.62	
C	652	0.035398	-0.16991	1.7	0.2107	14.0368	0.00	91.62	8393.95
	341	0.04335	-0.20808	1.72	0.2539	13.8287	0.28	91.90	8445.47
	342	0.072507	-0.34803	1.82	0.3898	13.4807	1.38	93.28	8701.55
	343	0.072516	-0.34808	1.92	0.3550	13.1326	1.35	94.63	8954.87
	344	0.072518	-0.34809	2.02	0.3202	12.7845	1.31	95.94	9205.14
	345	0.072518	-0.34809	2.12	0.2854	12.4365	1.28	97.22	9452.10
	346	0.072518	-0.34809	2.22	0.2506	12.0884	1.24	98.47	9695.46
	347	0.072518	-0.34809	2.32	0.2158	11.7403	1.21	99.67	9934.98
	348	0.072518	-0.34809	2.42	0.1810	11.3922	1.17	100.85	10170.40
	349	0.072518	-0.34809	2.52	0.1462	11.0441	1.14	101.99	10401.48
	350	0.072518	-0.34809	2.62	0.1114	10.6960	1.10	103.09	10627.97
	351	0.072516	-0.34808	2.72	0.0766	10.3479	1.07	104.16	10849.65
	352	0.072507	-0.34803	2.82	0.0418	9.9999	1.03	105.20	11066.29
	353	0.04335	-0.20808	2.92	0.0042	9.7918	1.00	106.20	11277.68
Dy	605		-67.2168	2.94	0.0000	-57.4250	0.20	106.39	
D	605	0.035398	-0.16991	2.94	0.0000	-57.5949	0.00	106.39	11319.31
	354	0.085668	-0.41121	3.03	-0.0370	-58.0061	-5.18	101.21	10243.20
	355	0.115708	-0.5554	3.13	-0.1055	-58.5615	-5.80	95.41	9102.71
	356	0.132445	-0.63574	3.23	-0.1844	-59.1972	-5.86	89.55	8019.55
	357	0.144202	-0.69217	3.33	-0.2699	-59.8894	-5.92	83.63	6994.35
	358	0.155976	-0.74868	3.43	-0.3669	-60.6381	-5.99	77.64	6028.48
	359	0.167748	-0.80519	3.53	-0.4751	-61.4433	-6.06	71.58	5123.62
	360	0.179515	-0.86167	3.63	-0.5946	-62.3049	-6.14	65.44	4281.76
	361	0.191282	-0.91815	3.73	-0.7253	-63.2231	-6.23	59.20	3505.19
	362	0.188155	-0.90314	3.83	-0.8038	-64.1262	-6.32	52.88	2796.55
	363	0.164738	-0.79074	3.93	-0.7828	-64.9170	-6.41	46.47	2159.44
	364	0.141204	-0.67778	4.03	-0.7388	-65.5947	-6.49	39.98	1598.24
	365	0.11767	-0.56482	4.13	-0.6721	-66.1596	-6.56	33.42	1116.80
	366	0.094135	-0.45185	4.23	-0.5829	-66.6114	-6.62	26.80	718.38
	367	0.0706	-0.33888	4.33	-0.4710	-66.9503	-6.66	20.14	405.68
	368	0.04706	-0.22589	4.43	-0.3366	-67.1762	-6.70	13.45	180.81
	369	0.023372	-0.11219	4.53	-0.1784	-67.2884	-6.72	6.73	45.28
E	370	0.040216	-0.19304	4.63	-0.3262	-67.4814	-6.73	0.00	0.00
Ey	370		67.4814	4.63	114.0436	0.0000	0.00	0.00	0.00
	SUM		0.0000	SUM	0.0000			SUM	256796
								ΣM²/(2EI)	2.68
								TOTAL ΣM²	2170074.3
								TOTAL STRAIN ENERGY OF ENTIRE GRID	22.62
								Mmax [kNm]	106.39
								Vmax [kN]	58.20
								Vmin [kN]	-67.48